SANDIA REPORT

SAND2007-6686
Unlimited Release
Printed October 2007

THz Quantum Cascade Lasers for Standoff Molecule Detection

MIchael Wanke
Maytee Lerttamrab
Ines Waldmueller
Weng Chow

Prepared by
Sandia National Laboratories
Albuquerque, New Mexico 87185 and Livermore, California 94550

Sandia is a multiprogram laboratory operated by Sandia Corporation,
a Lockheed Martin Company, for the United States Department of Energy's
National Nuclear Security Administration under Contract DE-AC04-94-AL85000.

Sandia National Laboratories

Issued by Sandia National Laboratories, operated for the United States Department of Energy by Sandia Corporation.

Available to DOE and DOE contractors from
U.S. Department of Energy
Office of Scientific and Technical Information
P.O. Box 62
Oak Ridge, TN 37831

Telephone: (865) 576-8401
Facsimile: (865) 576-5728
E-Mail: reports@adonis.osti.gov
Online ordering: http://www.osti.gov/bridge

Available to the public from
U.S. Department of Commerce
National Technical Information Service
5285 Port Royal Rd
Springfield, VA 22161

Telephone: (800) 553-6847
Facsimile: (703) 605-6900
E-Mail: orders@ntis.fedworld.gov
Online ordering: http://www.ntis.gov/help/ordermethods.asp?loc=7-4-0#online

SAND2007-6686
Unlimited Release
Printed October 2007

THz Quantum Cascade Lasers for Standoff Molecule Detection

Michael C. Wanke and Maytee Lerttamrab
Photonics Microsystems Technologies Department

Weng Chow and Ines Waldmueller
Semiconductor Materials and Device Sciences Department

Sandia National Laboratories
P.O. Box 5800
Albuquerque, NM 87185-1181

Abstract

Remote optical detection of molecules, agents, and energetic materials has many applications to national security interests. Currently there is significant interest in determining under what circumstances THz frequency coverage will aid in a complete sensing package. Sources of coherent THz frequency (i.e. 0.1 to 10 THz) electromagnetic radiation with requisite power levels, frequency agility, compactness and reliability represent the single greatest obstacle in establishing a THz technology base, but recent advances in semiconductor-based quantum cascade lasers (QCLs) offer huge improvements towards the ultimate THz source goals. This project advanced the development of narrow-linewidth THz quantum cascade lasers. We developed theoretical tools to guide the improvement of standard THz quantum cascade lasers, the investigation of nonlinear optics employing infrared QCLs, and the exploration of quantum coherence to improve QCL performance. The latter was aimed especially towards achieving high temperature operation. In addition we developed a computer algorithm capable of shifting the frequencies of an existing THz QCL to a different frequency and invented a new type of laser that may enable room temperature THz generation in a electrically driven solid-state source.

Acknowledgment

Many people contributed to this project. In no particular order I would like to thank John Reno, Larry Stephenson, and Terry Hargett for the MBE growth of a large number of THz QCLs, Sally Samora, Chris Apblett, Gerry Gerard, Mike Cich, Amelia Sanchez, and Bandwidth Semiconductor Inc., for processing the laser material into functional devices, Chuck Fuller, Yelena Berliba,Todd Barrick, and Erik Young for sample preparation and measurements, Steve Gentry, Andy Boye and Toby Townsend for supporting the effort to pursue the long term potential of THz technologies, and Mark Lee, Igal Brener, and Eric Shaner for many helpful scientific and motivation support discussions.

Contents

List of Figures

List of Tables

Summary

This project expanded the capabilities to model and simulate quantum cascade lasers (QCLs). and moved Sandia closer to the point of being able to predict laser performance from first principles. We developed an in house capability and expanded on previous work in the field for predicting laser characteristics such as population inversion, voltage-current relations, and gain spectra, and went significantly beyond others by developing a microscopic theory to account for the non-linear interaction between the laser field and the active medium. With these tools we investigated the dependence of the laser performance on issues such as temperature, doping, and material characteristics (e.g. non-parabolicity), to begin guiding the development of higher power, higher temperature lasers.

We also invented and explored a new type of QCL structure that is both optically and electrically pumped. Theoretical results for this design predict room temperature THz generation. The overall desire is to have a completely electrically driven THz source, and an optical pump seems to be contradictory to this desire, but the required pump energies are easily achieved by mid-infrared QCLs which can be incorporated into the structure to yield a true two terminal electronic THz source. The exploration of this concept led to the unexpected and pleasant discovery that this structure may be an ideal material to explore and harness quantum coherence effects in semiconductors.

In addition, we developed a design algorithm and implemented it into our laser design codes to take known laser structures and redesign them automatically to any other frequency that we desire. This reduced the time it takes to develop a laser at a new frequency from days to a few minutes. For sensing purposes this allows us to tailor lasers quickly to operate at frequencies corresponding to the molecular absorption features of interest to a particular application.

Beside the knowledge and capability gained during the work, the project resulted in 1 technical advance, 4 refereed journal articles, 7 conference presentations, 6 conference proceedings, provided the underpinnings of the THz Grand Challenge, led to a new type of laser (OPED), spawned a new LDRD to explore the new frontiers for quantum optics enabled by optically pumped, electrically biased structures, supported training of 2 postdocs, 1 limited term employee, and 2 students (1 graduate and 1 undergraduate), and initiated multiple external collaborations.

Publications

I. Waldmueller, W. W. Chow, A. Knorr, Influence of radiative coupling on coherent

Rabi intersubband oscillations in multiple quantum wells, Physical Review B 73 (3), 035433, January 2006

I. Waldmueller, W.W. Chow, E.W. Young, M.C. Wanke, Nonequilibrium many-body theory of intersubband lasers, Journal of Quantum Electronics 42 (3), 292, March 2006

I. Waldmueller, W.W. Chow, and M.C. Wanke, Optically-pumped electrically-driven THz generation - an approach for an efficient THz Quantum Cascade Laser?, Journal of Quantum Electronics (Special Topics), July/August 2007

I. Waldmueller, M.C. Wanke, and W.W. Chow, Circumventing the Manley-Rowe quantum efficiency limit in an optically pumped terahertz quantum-cascade amplifier, Phys. Rev. Lett. 99, 117401, September 2007

Conference Publications / Presentations

Paper and poster presentation: Semiclassical many-body theory of Quantum-Cascade Lasers, ITQW 2005

Paper and oral presentation: Linear and Nonlinear Responses of Intersubband Lasers, CTuFF6, CLEO 2006

Paper and oral presentation: Influence of Radiative Coupling on the Nonlinear Optical Response of Intersubband Transitions in Multiple Quantum Wells, QMK6, CLEO 2006

Paper and poster presentation: Gain without inversion: an approach for THz Quantum Cascade Laser?, ISLC 2006

Paper and oral presentation: Optically-assisted electrically-driven THz generation - a new approach for efficient THz Quantum Cascade Lasers?, CLEO 2007

Oral presentation: Optically-pumped electrically-driven THz generation - a new approach for efficient THz Quantum Cascade Lasers?, IEEE/LEOS Semiconductor Laser Workshop 2007

Invited Oral Presentation: Advances in Terahertz Technology and Microsystems. LASERION 2007

Poster presentation, Characterization of Terahertz Quantum Cascade Lasers, Sandia Student Symposium

Paper and oral presentation: Who needs population inversion? Automatically phase-matched quantum coherence contributions as a source for THz radiation, ITQW 2007

Nomenclature

QCL Quantum Cascade Laser

OPED Optically pumped, electrically driven laser

MBE Molecular Beam Epitaxy

THz Short for terahertz – (10^{12} cycles/sec)

MIR Mid-infrared

FIR Far-infrared

dc direct current

ac alternating current

LO phonon - longitudinal optical phonon. The strongest non-radiative relaxation mechanism in quantum cascade lasers.

Chapter 1

Introduction

The recent development of semiconductor based THz QCLs has opened the door to compact, robust THz sources. The first THz QC laser (4.5 THz) was reported in 2002 [1]. This laser was extrapolated from a long-wave IR design based on chirped superlattice structures. Since then more design concepts have been adapted from successful mid-infrared designs: bound-to-continuum [2], resonant-phonons [3], and alternating photon-phonon regions [4]. Theoretical modeling has mostly been limited to carrier transport [5] [17] but little has been done to explore the carrier-light interaction.

The performance of the current generation of QCLs in terms of power, operating temperature, and lasing at chosen wavelengths are key issues which were studied intensively as part of this proposed effort. At the beginning of this project, THz QCLs were designed mostly by intuition learned from designing mid-infrared QCLs. To really optimize the performance requires understanding the electron behavior inside the lasers especially in regards to knowing the energy level electron occupations and the radiative and non-radiative scattering rates between states. Without the capability to model these features, one cannot ensure the population inversion needed for lasing or more fundamentally calculate the actual bandstructure of the laser which is the fundamental basis for design.

We significantly advanced our numerical modeling tools to provide the capabilities to predict many of the important laser performance metrics. These tools included developing a completely self-consistent bandstructure code that can calculate the potential profile of the laser including Poisson corrections, determine the populations of every state in the structure, calculate the predicted current, model the gain of the active region, explore the carrier temporal dynamics, account of the interaction of the laser field back onto the electrons, and study quantum coherence in intersubband transitions. This work is covered in chapter 3.

With these new theoretical tools we were able to invent and model a new type of optically-pumped electrically driven (OPED) THz laser. This design was proposed to overcome the low operating temperatures of existing THz QCLs and the theoretical results look very promising towards room temperature operation. This new laser concept is described in chapter 4

For gas sensing applications it is important that the laser operate over a frequency

range that covers the desired molecular absorption lines of interest. Typical THz QC lasers can be tuned using various methods by up to a few hundred GHz. Therefore, in the near term, multiple lasers will be needed to cover multiple gas species. Designing new lasers from scratch is time intensive, and therefore we also developed a computer algorithm that can take an existing laser design and shift it to a new frequency (in a matter of minutes). This is described in chapter 5.

Experimental testing was supposed to proceed alongside the theoretical developments to provide feedback for improving the models. Unfortunately, 1 year into the project our ability to grow the laser material was temporarily shut down to move the machines to a new building. While this was supposed to take about 6 months, it was not until late in the third year that growth was re-established and the material quality is still inferior to pre-move levels. Processing variations resulting from the move to a new fabrication facility also led to strong sample to sample variation during the moving process. Thus the current quality of the resulting lasers is not adequate for comparing to the models so only gross effects could be demonstrated, such as verifying the frequency shifting algorithm. Therefore the majority of this report will describe the theoretical and modeling capability enhancements.

Chapter 2

Theory and modeling Introduction

Quantum cascade lasers (QCLs) have become an important topic during the last decade. Based on transitions between conduction subbands, QCLs have been fabricated for a wide range of infrared frequencies. Recently, significant interest has focused on the development of QCLs in the THz regime [1]. In conventional QCLs, carriers are injected directly into the energetically higher laser subband (see for example Fig.2.1). In the case of THz QCLs, the lower laser subband is depleted into a miniband of states [1], by an interlaced photon-phonon cascade [4], by bound-continuum transitions [7] or by single [3] or double resonant optical-phonon scattering [8]. At low temperature, these depletion mechanisms are sufficiently efficient to yield population inversion with relatively low threshold. However, temperature dependent scattering processes (parasitic current channels) and thermal backfilling destroy the population inversion at high temperature [9]. As a result, lasing threshold of direct QCLs in the THz regime increases appreciably with increasing temperature, limiting the present maximum operation temperature to 164 K [10]. To meet the challenge of providing efficient THz sources for the low and especially high temperature regime, it appears plausible to focus not only on the improvement of conventional QCL designs, but also to explore conceptually new approaches for THz QCLs, as for example the optically-pumped electrically driven THz QCL (see Fig. 2.2). In chapter 3, we present the theoretical work on conventional (direct) QCLs, and in chapter 4, the results of our research on conceptually new approaches for THz QCLs.

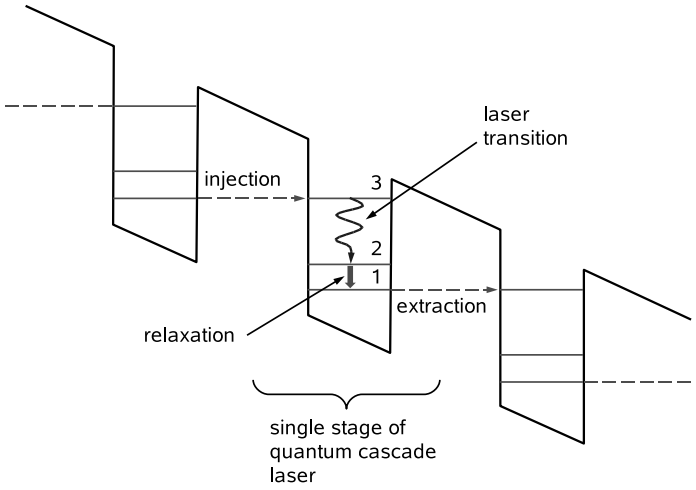

Figure 2.1. Simple cartoon of a three repeated unit cells of a direct QCL with single optical-phonon depletion: Carriers are injected into subband 3, lasing transitions occur between subbands 3 and 2, electron-phonon scattering depletes subband 2. In a QCL laser the carriers depleted from subband 1 are injected in subband 3 of the next stage. The real structure will have mulitple wells per period.

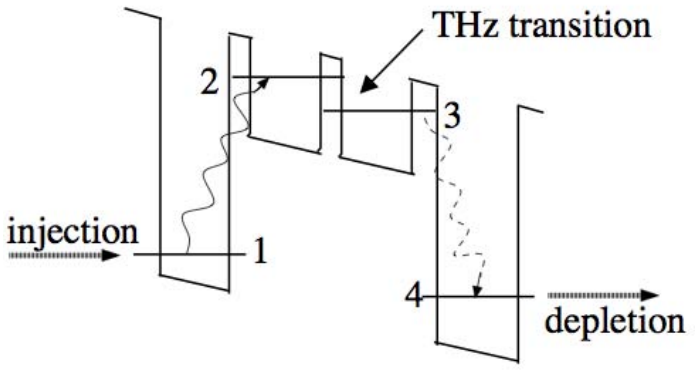

Figure 2.2. Single stage of proposed optically-pumped electrically-driven THz QCL as conceptually new approach for THz quantum cascade laser. Without pump recovery (dashed transition), the scheme reverts to a conventional optical conversion configuration.

Chapter 3

Modeling Conventional (Direct) QCL to Improve Understanding and Performance

With the rapid experimental development of quantum cascade lasers, the need for predictive laser models is obvious. In the past, much effort has been made to develop theories and models for investigating different aspects of intersubband laser behavior [11]-[28]. Presently, the attention is focused mainly on the transport mechanisms. In the past years, a variety of theoretical models for conventional QCLs were proposed: using either Monte Carlo simulations [11, 5, 16, 19, 21, 23, 28], nonequilibrium Green functions [12, 17, 20, 25, 26, 27] or the kinetic energy balance method (rate equation model) [13, 14, 15, 18]. Gain spectra, population inversion and voltage-current characteristics of different laser structures were predicted and successfully compared with experimental results.

For efficient development of QCLs it is crucial to have access to in-house predictive laser models. With the goal to obtain in-house capabilities for the prediction of the steady-state behavior of conventional QCL designs (population inversion, voltage-current, etc.), we first implemented a time-independent self-self consistent QCL model (see chapter 3.1). However, all time-independent models as well as existing time dependent models [see for example [22, 16, 24]] that can investigate ultrafast carrier dynamics can not describe nonlinear response, because the evolution of the laser field is not taken into account. For this reason, we additionally developed a microscopic theory, which considers the nonlinear interaction between the laser field and active medium of intersubband lasers (see chapter 3.2). A combination of both models yields a complete laser model, suitable for investigating both steady-state as well as dynamical laser characteristics.

3.1 Self-Self-Consistent Steady-State QCL Model

Similar to proposed models by Harrison et al. [see e.g. [13, 14, 18]], the self-self-consistent steady-state model iteratively determines the solution of the Schrdinger

Equation, the solution of the Poisson Equation, the lifetimes/scattering rates and the corresponding steady-state carrier-distribution. Figure 3.1 shows a schematic drawing of the self-self-consistent model.

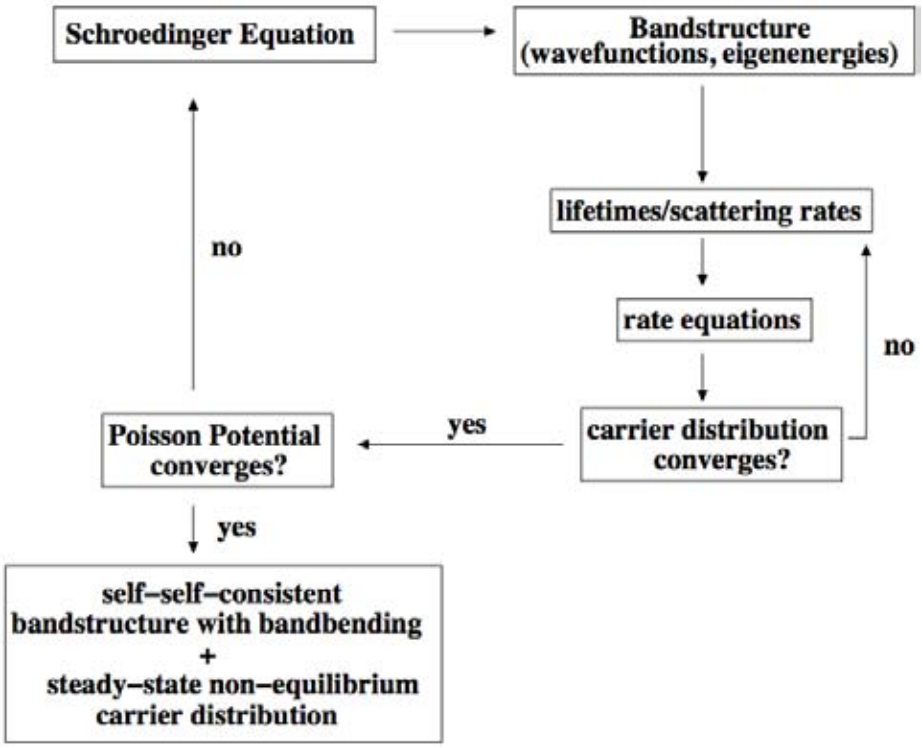

Figure 3.1. Flowchart of self-self-consistent calculation of bandstructure (with bandbending effects) and steady-state time-independent non-equilibrium carrier-distribution.

3.1.1 Part I: Bandstructure Calculation

With design specifications (materials, layer thickness, bias) as input parameters, the implemented program first solves Schrdinger's Equation for the undoped sample following a concept developed by Winkler et al. [29, 30].

Starting from an 8x8 bulk Hamiltonian (lowest conduction band, heavy hole, light hole and split-off band, each being twice spin degenerate), we derive the corresponding heterostructure Hamiltonian $H(z)$ in position space by replacing the kinetic energy operator according to

$$k_z A \rightarrow \frac{1}{2}[(-\mathrm{i}\partial_z)\mathrm{A}(\mathrm{z}) + \mathrm{A}(\mathrm{z})(-\mathrm{i}\partial)] \,, \tag{3.1}$$

$$Ak_z^2 \rightarrow (-\mathrm{i}\partial_z)\mathrm{A}(\mathrm{z})(-\mathrm{i}\partial_z) \,. \tag{3.2}$$

In order to solve the eigenvalue problem:

$$H(z)\Psi(z) = \epsilon\Psi(z)\,, \tag{3.3}$$

we switch over to momentum space. A Fourier transform of Eq. 3.3 leads to the coupled integral equations

$$H(k)\Psi(k) \equiv \int_{-\infty}^{\infty} dk'_z H(k_z - k'_z)\Psi(k'_z) = \epsilon\Psi(k_z)\,. \tag{3.4}$$

In Eq. 3.4, the matrix $H(k_z - k'_z)$ has been obtained from the heterostructure $\mathbf{k}\cdot\mathbf{p}$-matrix by replacing

$$[(-\mathrm{i}\partial_\mathrm{z})^\mathrm{m}\mathrm{A}(\mathrm{z}) + \mathrm{A}(\mathrm{z})(-\mathrm{i}\partial)^\mathrm{m}] \;\rightarrow\; (k_z^m + k_z'^m)A(k_z - k'_z)\,, \tag{3.5}$$

$$(-\mathrm{i}\partial_\mathrm{z})^\mathrm{m}\mathrm{A}(\mathrm{z})(-\mathrm{i}\partial_\mathrm{z})^\mathrm{m} \;\rightarrow\; (k_z k'_z)^m A(k_z - k'_z)\,, \tag{3.6}$$

where $A(k_z)$ is the Fourier transform of $A(z)$.

A concept based on a quadrature method for the coupled integral equations in momentum space is then used to determine the eigenvalues of the system. Fourier transformation of the calculated eigenvalues yields the bandprofile (wavefunctions and eigenenergies) of the undoped sample in position space. As an example, Fig. 3.2 shows the calculated bandstructure of an undoped GaAs/AlGaAs QCL.

3.1.2 Part II: Scattering Rates/Lifetimes and Carrier Distribution

In the next part, the calculated bandprofile of the undoped sample serves as input for the calculation of lifetimes and scattering rates.

The lifetimes and scattering rates depend on the actual carrier distribution in the sample, which at this point of the calculation is unknown. Therefore, as the starting condition all subbands are assumed to be equally occupied.

Assuming that each period of the QCL behaves in the same manner, we derive rate equations for the states located in the center stage(s) of the QCL (original states). The rate equations for these subbands describe the carrier transfer in the center stage(s) of the system. In order to account for the electron flow in the cascaded system, i.e. to consider electron flow between the center stage(s) and neighboring stages, we follow Indjin et al. [18] and introduce periodic boundary conditions. We rewrite the rate

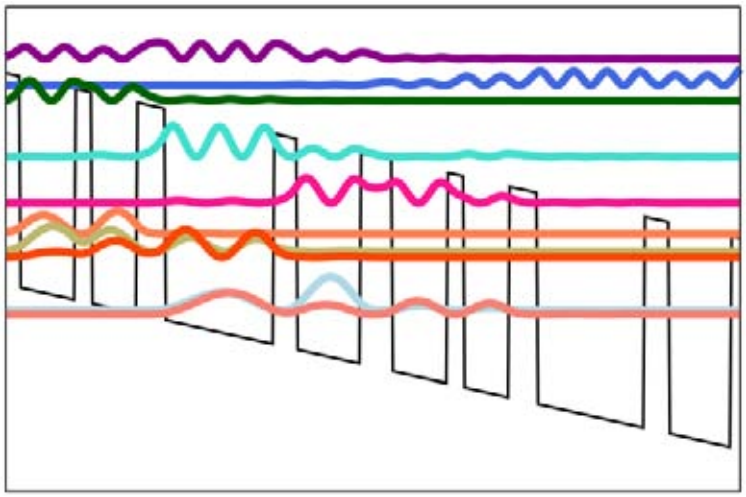

Figure 3.2. Calculated bandstructure for undoped GaAs/AlGaAs QCL. The black line represents the potential profile created by the heterostructure design. High values correspond to AlGaAs barriers while low values correspond to GaAs well. The slope accounts for the applied dc electrical bias.

equations so that carriers are cycled around $2\times A$ states for A original states:

$$\frac{d}{dt}n_i = \sum_{m=1}^{2A}(\gamma_{mi}n_m - \gamma_{im}n_i) + \sum_{m=1}^{A}(\gamma_{mi+A}n_m - \gamma_{i+Am}n_i) \quad (3.7)$$

$$\frac{d}{dt}n_{i+A} = \sum_{m=1}^{2A}(\gamma_{mi+A}n_m - \gamma_{i+Am}n_{i+A}) + \sum_{m=1}^{A}(\gamma_{m+Ai}n_{m+A} - \gamma_{im+A}n_{i+A}) \quad (3.8)$$

for $i = 1, .., A$. States $1..A$ are the original states, states $A+1...2A$ are the corresponding duplicates (same state, but centered in neighboring stage, the wavefunctions are shifted by the width of one period and the eigenenergies by the energy drop in one period). γ_{im} denotes the scattering rate between subbands i and m, n_i the subband occupation of subband i. After calculating the scattering rates for the $2 \times A$ states with initial equal subband occupation, the actual carrier distribution is determined by the steady-state solution of the rate equations. The new carrier distribution is then used to calculate new scattering rates and the process is repeated until the carrier distribution converges. As an example for the iterative determination of the actual carrier distribution, we plot in Fig. 3.3 the evolution of the subband occupations with iteration number.

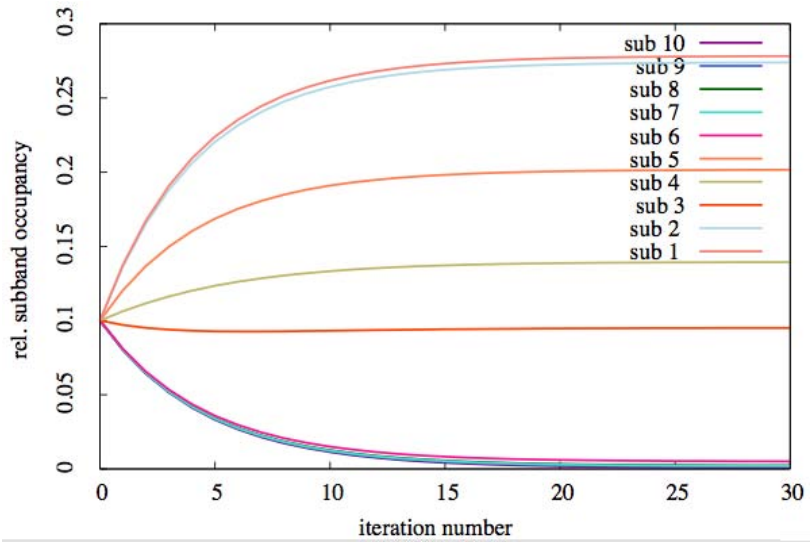

Figure 3.3. Convergence of subband occupation due to self-consistent calculation of lifetimes/scattering rates and carrier distribution. The subbands correspond to the 10 states shown in Fig. 3.2

.

3.1.3 Part III: Poisson Potential

Once the level occupations are known we can calculate the electron density as a function of position, and typically this will not correspond to position of the dopants grown in the material. Therefore, there will be built in electric fields between the electrons and ionized dopants which will effect the potential distribution. By solving Poisson's Equation,

$$\nabla^2 V_\rho = -\frac{\rho}{\epsilon}\,, \tag{3.9}$$

we determine the potential V_ρ due to the charge density ρ in the doped sample

$$V_\rho(z) = -\int_{-\infty}^{z} E(z)dz \tag{3.10}$$

$$= -\int_{-\infty}^{z} dz \sum_{z'=-\infty}^{\infty} \frac{\sigma(z')}{2\epsilon} sign(z-z')\,. \tag{3.11}$$

Since the laser potential is effectively 1- dimensional, we can assume that the charge density ρ can be thought of as an infinite plane, i.e. a sheet, with areal charge density

$\sigma(z)$ (per stage) and thickness δ_z:

$$\sigma(z) = q[\sum_{i=1}^{n} N_i \psi_i^*(z)\psi_i(z) - d(z)]\delta_z \; . \tag{3.12}$$

N_i denotes the $2d-$ carrier density of subband i, $N = \sum_{i=1}^{n} N_i = \int_{-\infty}^{\infty} d(z)\delta_z$ the $2d-$ carrier density per stage, $d(z)$ the $3d$ carrier density, i.e. the z-dependent doping profile, and $\psi(z)$ the wavefunction of subband i. The potential resulting from the charge inhomogeneity in the QCL is then added to the confinement potential due to the conduction-band discontinuity and bias electric field in the Schrödinger Equation which yields the inclusion of bandbending effects due to charge distribution. The impact of the free carrier charge distribution shown in Fig. 3.3 on the bandstructure can be seen by comparing the bandprofile of the doped sample shown in Fig. 3.4 with the bandprofile of the undoped sample presented in Fig. 3.2.

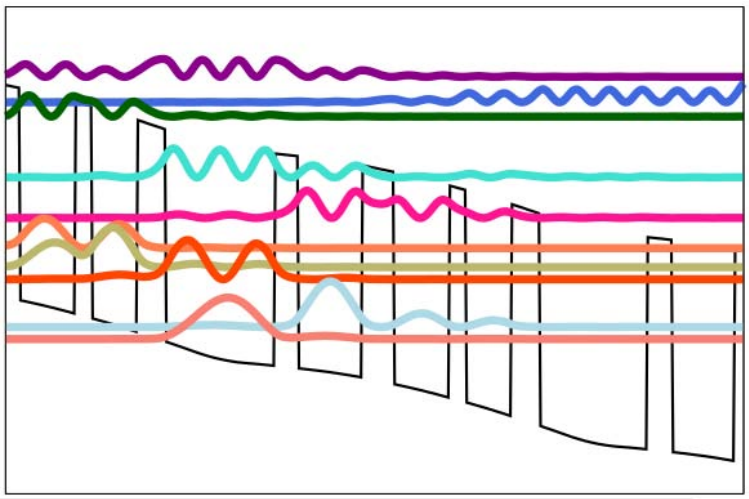

Figure 3.4. Calculated bandstructure for doped GaAs/AlGaAs QCL including band-bending effects resulting from the charge distribution as shown in Fig. 3.3

.

3.1.4 Self-Self-Consistent Bandprofile and Carrier Distribution

Iterative solving of parts I-III, yields the bandstructure with respect to bandbending effects, the lifetimes/scattering rates and the steady-state carrier-distribution. The final bandprofile and carrier-distribution for the structure shown in Figs. 3.2-3.4 is given in Fig. 3.5.

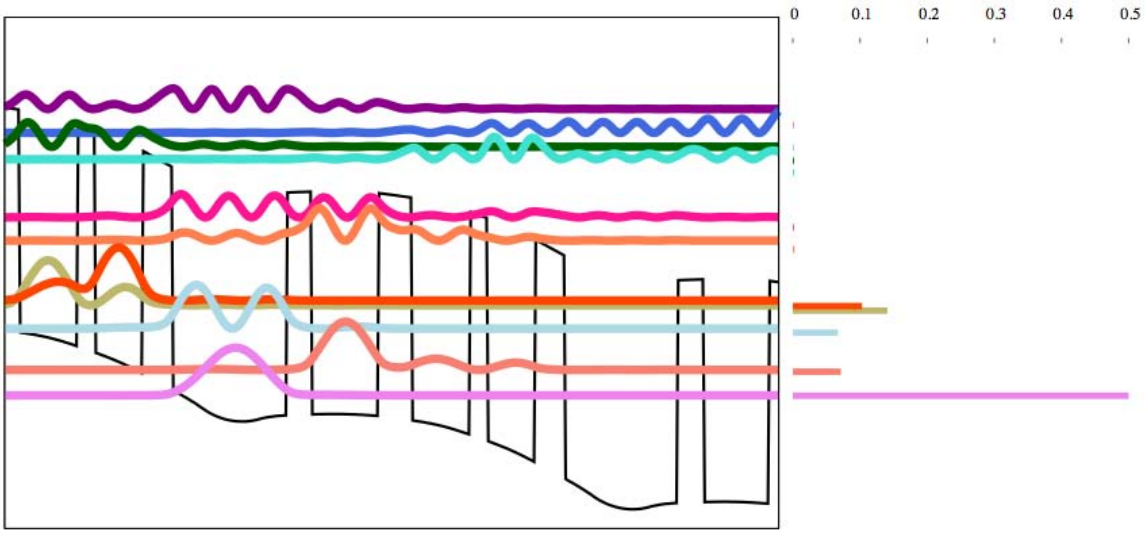

Figure 3.5. Final self-self-consistent bandprofile and carrier-distribution for doped sample [compare Fig. 3.2-3.4]. In steady-state half of the carriers are located in the lowest subband

This information is the basis for the determination of steady-state laser characteristics such as voltage-current relation and modal gain. All the derivations above include the dependence on the temperature of the laser, and therefore the operating temperature can be taken into account for laser design and performance predictions.

3.1.5 Steady-state Laser Characteristics: Current Calculation

The current density is one of the steady-state laser characteristics which can be determined based on the self-self-consistent bandprofile and carrier distribution calculated in chapter 3.1.4. The current density is evaluated by accounting for all carriers which pass through a reference plane, e.g. the interface between two stages (periods) of a QCL or in terms of periodic boundary conditions, the carriers which pass between original and duplicate states. After calculating the bandprofile and carrier distribution for a given electrical bias and operation temperature, the corresponding current is thus given by

$$J = q \sum_{i=1}^{A} \sum_{m=A+1}^{2A} \left(\gamma_{im} n_i - \gamma_{mi} n_m \right) . \tag{3.13}$$

This result has a very similar shape and temperature dependence to what is observed in actual laser structures.

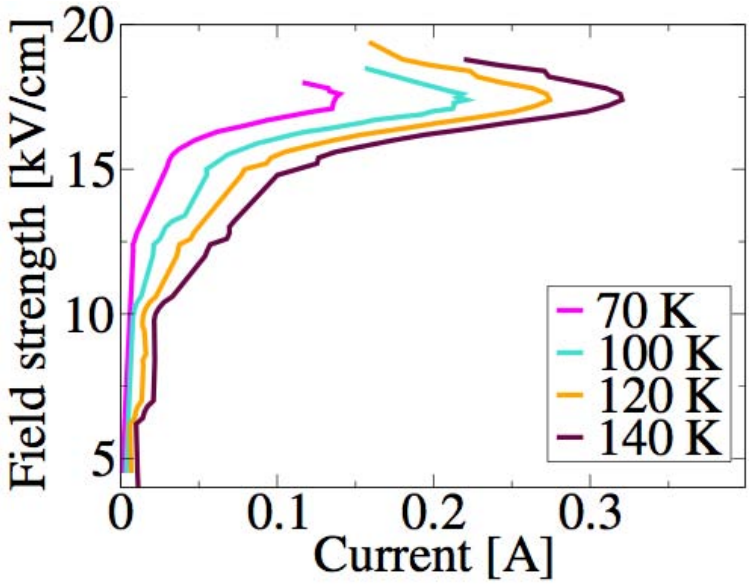

Figure 3.6. Dependence of current density on applied bias and operation temperature for the example of an GaAs/AlGaAs QCL.

3.2 Dynamical Many-Body Theory for Intersubband Laser

By simultaneously solving Maxwell's equations for the laser field and the semiconductor Bloch equations for the gain medium, the linear and nonlinear response of an intersubband laser can be investigated. In addition to first-order many-body contributions (Hartree-Fock), second order many-body contributions (scattering) are taken into account by connecting the laser theory to a microscopic treatment of carrier-carrier and carrier-phonon scattering. As an application of the theory, we present here the response of a three-subband laser which incorporates the main features of one stage of an active region of a QCL (see Fig. 2.1).

3.2.1 Theoretical Background

Our theoretical approach is based on the Maxwell-semiconductor Bloch equations for the laser field and gain medium. In the example presented here, the gain region consists of a single quantum well with three subbands as depicted in Fig. 2.1. Carriers are injected in the highest energy subband (subband 3) where they undergo a laser transition to a lower subband (subband 2). Carrier-phonon scattering then transfers carriers from subband 2 to subband 1.

3.2.2 Description of Laser Field

Assuming single-mode operation, the laser field is written as

$$E(\mathbf{r},t) = \frac{1}{2}\mathcal{E}(t)u(\mathbf{r})\mathrm{e}^{-\mathrm{i}[\omega \mathrm{t}+\phi(\mathrm{t})]} + c.c.\,, \tag{3.14}$$

where, $u(\mathbf{r})$ denotes the passive eigenfunction of the laser cavity at frequency ω, $\mathcal{E}(t)$ is the real field amplitude and ϕ is the phase. The temporal development of the laser field $E(t)$ is determined by solving the reduced wave equations (in SI units):

$$\frac{d}{dt}\mathcal{E}(t) = -\gamma_c\,\mathcal{E}(t) - \frac{\omega\Gamma}{\epsilon_0\epsilon_B V_{QW}} Im[\sum_{\mathbf{k}} d_{23}p^{23}_{\mathbf{k}}(t)] \tag{3.15}$$

$$\frac{d}{dt}\phi(t) = -\frac{\omega\Gamma}{\epsilon_0\epsilon_B V_{QW}\mathcal{E}(t)} Re[\sum_{\mathbf{k}} d_{23}p^{23}_{\mathbf{k}}(t)] \tag{3.16}$$

where γ_c denotes the cavity linewidth and $\Gamma = (\int_{QW} d^3r|u(\mathbf{r})|^2)/(\int_C d^3r|u(\mathbf{r})|^2)$ is the confinement factor, which gives the ratio of the mode in the quantum well (QW) and the cavity (C). V_{QW} is the volume of the quantum well. ϵ_B is the background

permittivity, ϵ_0 is the vacuum permittivity and d_{23} is the dipole matrix element with envelope wave function $\psi_i(z)$ of subband i and (negative) electron charge e

$$d_{23} = e\int dz\psi_2(z)z\psi_3(z)\,. \tag{3.17}$$

The intersubband coherence at $2D$-wave number $\mathbf{k}$ is denoted by $p^{23}_{\mathbf{k}} = \langle a^\dagger_{2,\mathbf{k}} a_{3,\mathbf{k}}\rangle$, where $a^\dagger_{i,\mathbf{k}}$ ($a_{i,\mathbf{k}}$) represents the creation (annihilation) of an electron with wave number $\mathbf{k}$ in subband i.

3.2.3 Description of Gain Medium

Starting from the Robertson equation [31] and the Hamiltonian of the system we derive the equations for intersubband coherence, $p^{23}_{\mathbf{k}} = \langle a^\dagger_{2,\mathbf{k}} a_{3,\mathbf{k}}\rangle$, and electron occupation numbers in subband i, $n_{i,\mathbf{k}} = \langle a^\dagger_{i,\mathbf{k}} a_{i,\mathbf{k}}\rangle$. In the Hamiltonian, we include terms for the energies of the noninteracting electrons and longitudinal-optical (LO) phonons, the carrier-field interaction, the Coulomb interaction of the electronic system, and the electron–LO-phonon interaction [32]. The derivation of the equations of motions for a two subband system can be found in [33]. For the three subband laser presented in Fig. 2.1, the equations of motion are given by

$$\frac{d}{dt}p^{23}_{\mathbf{k}} = \frac{\mathrm{i}}{\hbar}(-\tilde{\epsilon}_{32,\mathbf{k}} + \hbar\omega + \hbar\,\frac{d}{dt}\phi_L(t))p^{23}_{\mathbf{k}} + \mathrm{i}\tilde{\Omega}(\mathrm{t})(\mathrm{n}_{2,\mathbf{k}} - \mathrm{n}_{3,\mathbf{k}}) + \left.\frac{\mathrm{d}}{\mathrm{dt}}\mathrm{p}^{23}_{\mathbf{k}}\right|_{\mathrm{scatt}} \tag{3.18}$$

$$\frac{d}{dt}n_{1,\mathbf{k}} = -\Lambda + \left.\frac{d}{dt}n_{1,\mathbf{k}}\right|_{\mathrm{scatt}} \tag{3.19}$$

$$\frac{d}{dt}n_{2,\mathbf{k}} = -\mathrm{i}[\tilde{\Omega}(\mathrm{t})\mathrm{p}^{32}_{\mathbf{k}} - \mathrm{c.c.}] + \left.\frac{\mathrm{d}}{\mathrm{dt}}\mathrm{n}_{2,\mathbf{k}}\right|_{\mathrm{scatt}} \tag{3.20}$$

$$\frac{d}{dt}n_{3,\mathbf{k}} = \Lambda + \mathrm{i}[\tilde{\Omega}(\mathrm{t})\mathrm{p}^{32}_{\mathbf{k}} - \mathrm{c.c.}] + \left.\frac{\mathrm{d}}{\mathrm{dt}}\mathrm{n}_{3,\mathbf{k}}\right|_{\mathrm{scatt}}\,. \tag{3.21}$$

$\tilde{\epsilon}_{32,\mathbf{k}}$ is the $\mathbf{k}-$dependent transition energy between the two laser subbands modified by the corresponding many-particle contribution (exchange shift (HF,I)):

$$\tilde{\epsilon}_{32,\mathbf{k}} = \epsilon_{3,\mathbf{k}} - \epsilon_{2,\mathbf{k}} - \epsilon_{HF,I}(t) \qquad \text{with} \qquad \epsilon_{HF,I}(t) = \sum_{\mathbf{q}}\sum_{a=1}^{3} n_{a,\mathbf{q}}(t)[V^{3aa3}_{\mathbf{k}-\mathbf{q}} - V^{a22a}_{\mathbf{k}-\mathbf{q}}]\,. \tag{3.22}$$

$\tilde{\Omega}(t)$ denotes the effective Rabi frequency of the laser field renormalized by two many-body contributions (excitonic contribution (HF, II) and depolarization effect (HF,

III)):

$$\begin{aligned}\tilde{\Omega}(t) &= \Omega(t) + \Omega_{HF,II}(t) + \Omega_{HF,III}(t) \\ &= \mathcal{E}(t)d_{23} - \frac{1}{\hbar}\sum_{\mathbf{q}} V^{3232}_{\mathbf{k}-\mathbf{q}} p^{23}_{\mathbf{q}}(t) + \frac{2}{\hbar} V^{3223}_{0} \sum_{\mathbf{q}} p^{23}_{\mathbf{q}}(t)\end{aligned} \tag{3.23}$$

where $V^{abcd}_{\mathbf{q}}$ is the Coulomb matrix element

$$V^{abcd}_{\mathbf{q}} = \frac{1}{A}\frac{e^2}{2\epsilon_0}\frac{1}{q}\int dz \int dz' \mathrm{e}^{-q|z-z'|}\psi_a(z)\psi_b(z')\psi_c(z)\psi_d(z') \,. \tag{3.24}$$

We assume that the carriers are injected in subband 3 and depleted from subband 1 with a pump modeled via the injection (extraction) contribution:

$$\Lambda = \gamma(1 - n_{3,\mathbf{k}})n_{1,\mathbf{k}} \,. \tag{3.25}$$

In a QCL with several periods of active regions, the injection in the upper laser subband and depletion of carriers from the lowest subband would occur via scattering/tunneling of electrons between the various subbands in the active regions and injection regions.

The redistribution of the carriers between the three subband occurs as follows: the main part of the carriers in subband 3 makes a laser transition to subband 2. By including second-order carrier-carrier and carrier-phonon contributions (scattering contributions) into the theory, we take into account the possibility of relaxation from subband 3 to subband 2 or subband 1 by carrier-carrier or carrier-phonon interaction. As the contributions are rather lengthy, we discuss only their general structure and refer the reader to the appendix for the explicit formulas. The collision contributions for the intersubband coherence consist of diagonal terms, $\Xi_{\mathrm{d}}(p^{23}_{\mathbf{k}})$, dependent on the intersubband coherence at the same wave number, $p^{23}_{\mathbf{k}}$, and non-diagonal terms, $\Xi_{\mathrm{nd}}(\{p^{23}_{\mathbf{k}''}\})$, which couple intersubband coherences at different wave vectors:

$$\frac{d}{dt}p^{23}_{\mathbf{k}}|_{\mathrm{scatt,cc/cp}} = -\Xi_{\mathrm{d}}(p^{23}_{\mathbf{k}}) + \sum_{\mathbf{k}''\neq\mathbf{k}} \Xi_{\mathrm{nd}}(\{p^{23}_{\mathbf{k}''}\}) \tag{3.26}$$

with

$$\Xi_{\mathrm{d}}(p^{23}_{\mathbf{k}}) = \Gamma_{\mathrm{d}} p^{23}_{\mathbf{k}} = \frac{1}{2}\sum_i (\Gamma^{\mathrm{i,cp}}_{\mathrm{d}} + \Gamma^{\mathrm{i,cc}}_{\mathrm{d}}) p^{23}_{\mathbf{k}} \tag{3.27}$$

and

$$\sum_{\mathbf{k}''\neq\mathbf{k}} \Xi_{\mathrm{nd}}(\{p^{23}_{\mathbf{k}''}\}) = \sum_i \left[\sum_{\hat{\mathbf{q}}} \Gamma^{i,\mathrm{cp}}_{\mathrm{nd}}\ p^{23}_{\mathbf{k}+\hat{\mathbf{q}}_{||}} + \sum_{\mathbf{k}',\mathbf{q}} \Gamma^{i,\mathrm{cc}}_{\mathrm{nd1}}\ p^{23}_{\mathbf{k}'-\mathbf{q}} + \sum_{\mathbf{q}} \Gamma^{i,\mathrm{cc}}_{\mathrm{nd2}}\ p^{23}_{\mathbf{k}+\mathbf{q}} - \sum_{\mathbf{k}'} \Gamma^{i,\mathrm{cc}}_{\mathrm{nd3}}\ p^{23}_{\mathbf{k}'} \right] . \tag{3.28}$$

Here i goes over all subbands of the problem and $\hat{\mathbf{q}}$ denotes a 3D wave vector in contrast to the 2D wave vectors $\mathbf{k}, \mathbf{q}, \mathbf{k}', \mathbf{k}''$. The collision contributions for the population in subband a are given by:

$$\frac{d}{dt} n_{a,\mathbf{k}}|_{\text{scatt,cc/cp}} = -n_{a,\mathbf{k}} \Gamma_{\text{d,out}}^{\text{a,cc/cp}} + (1 - n_{a,\mathbf{k}}) \Gamma_{\text{d,in}}^{\text{a,cc/cp}} \,. \tag{3.29}$$

$\Gamma_{\text{d,in}}^{\text{i,cc/cp}}$ denotes the diagonal in-scattering and $\Gamma_{\text{d,out}}^{\text{i,cc/cp}}$ the corresponding diagonal out-scattering rate ($\Gamma_{\text{d}}^{\text{a,cc/cp}} = \Gamma_{\text{d,in}}^{\text{a,cc/cp}} + \Gamma_{\text{d,out}}^{\text{a,cc/cp}}$) due to carrier-carrier and carrier-phonon scattering, respectively.

In short, the scattering contributions given above introduce two effects:

1. In the population equations, they drive an existing non-equilibrium distribution of carriers into the corresponding quasi-equilibrium distribution.
2. In the equation for the intersubband coherence, the diagonal scattering contributions generally destroy the coherence between the laser levels, counteracted by the non-diagonal contributions which rebuild the coherence.

However, the evaluation of the scattering contributions at each time step requires lengthy computational time because of the number of $\mathbf{k}$-points necessary to ensure particle and energy conservation. For the following investigation of the laser properties of the intersubband laser, we will circumvent this problem by using the relaxation rate approximation. In this approximation, we assume that the impact of collision contributions on the carrier distributions can be modeled by the relaxation of a given population distribution $n_{i,\mathbf{k}}$ to a Fermi-Dirac distribution $f_{i,\mathbf{k}}(\mu_i, T_i)$) with chemical potential μ_i and temperature T_i [see for example [34]]. If carrier-carrier and carrier-phonon collisions occur on clearly distinguishable time-scales, carrier-carrier collisions drive the electrons towards a Fermi-Dirac distribution at plasma temperature ($\mu_i = \mu_{pl}$, $T_i = T_{pl}$). The actual values of the chemical potential and the plasma temperature can then be determined by the requirements of particle conservation

$$\frac{1}{A} \sum_{\mathbf{k}} \sum_{a} n_{a,\mathbf{k}} = \frac{1}{A} \sum_{\mathbf{k}} \sum_{a} f_{a,\mathbf{k}}(\mu_{pl}, T_{pl}) \tag{3.30}$$

and energy density conservation

$$\frac{1}{A} \sum_{\mathbf{k}} \sum_{a} \epsilon_{a,\mathbf{k}} n_{a,\mathbf{k}} = \frac{1}{A} \sum_{\mathbf{k}} \sum_{a} \epsilon_{a,\mathbf{k}} f_{a,\mathbf{k}}(\mu_{pl}, T_{pl}) \,, \tag{3.31}$$

where the index a runs over the subbands involved in the collisions. For example, the particle conservation for intrasubband collisions in subband i reads

$$\frac{1}{A} \sum_{\mathbf{k}} n_{i,\mathbf{k}} = \frac{1}{A} \sum_{\mathbf{k}} f_{i,\mathbf{k}}(\mu_{pl}, T_{pl}) \,, \tag{3.32}$$

for intersubband collisions between subbands $1, 2$ and 3

$$\frac{1}{A}\sum_{\mathbf{k}}\sum_{a=1}^{3} n_{a,\mathbf{k}} = \frac{1}{A}\sum_{\mathbf{k}}\sum_{a=1}^{3} f_{a,\mathbf{k}}(\mu_{pl}, T_{pl}) \,. \tag{3.33}$$

In the case of carrier-phonon collisions, energy is dissipated from the electrons to the lattice and the electrons relax to a Fermi-Dirac distribution at lattice temperature ($\mu_i = \mu_l$, $T_i = T_l$). Thus only the requirement of particle conservation remains:

$$\frac{1}{A}\sum_{\mathbf{k}}\sum_{a} n_{a,\mathbf{k}} = \frac{1}{A}\sum_{\mathbf{k}}\sum_{a} f_{a,\mathbf{k}}(\mu_{l}, T_{l}) \,. \tag{3.34}$$

where the energy exchange between carriers and lattice is taken into account by fixing the temperature of quasi-equilibrium to the lattice temperature [34]. If carrier-carrier and carrier-phonon collisions occur on similar time-scales, the electrons relax also to a Fermi-Dirac distribution at lattice temperature ($\mu_i = \mu_l$, $T_i = T_l$).

The effective rates for these relaxation processes are in general dependent on the structure (well width, carrier density, etc.) and on temperature. We determine the rates by microscopic investigations of the carrier-carrier and carrier-phonon collisions in the structure of interest: we calculate the relaxation of a given non-equilibrium distribution and compare the obtained results with calculations in the effective rate approximation. The effective polarization dephasing rate is determined via the absorption spectrum for transitions between laser subband 2 and 3. Therefore, the determined effective rate takes into account both the diagonal and the non-diagonal scattering contributions. More details, including a sample calculation, are given in Sec. 3.2.4.

For the numerical evaluation of the theory, we consider a single GaAs quantum well of width $L = 18$ nm, surrounded by $Al_{0.35}Ga_{0.65}As$ barriers. For simplicity we use a square-well potential model with a barrier height of $V_0 = 300$ meV. In most cases, QCLs are lightly doped with a carrier density between $n_e = 10^{10}$ cm^{-2} to $n_e = 6\times10^{11}$ cm^{-2}. We cover this range by examining two lasers with different carrier densities: $n_e = 6\times10^{11}$ cm^{-2} and $n_e = 5\times10^{10}$ cm^{-2}. However, as we are especially interested in the impact of many-body effects, which is supposed to increase with increasing carrier density, we investigate additionally a laser with a relatively high carrier density of $n_e = 1 \times 10^{12}$ cm^{-2}. In all cases the cavity linewidth is $\gamma_c = 0.5$ ps^{-1}. The impact of the nonparabolicity of the conduction band is taken into account according to Ekenberg in [36], i.e. we treat the energy dispersion of the subbands in effective mass approximation with mass m_i for subband i:

$$\epsilon_{i,\mathbf{k}} \;=\; \frac{\hbar k^2}{2\mathrm{m}_i} + \epsilon_{i,\mathbf{k}=0} \,. \tag{3.35}$$

For our structure we find $\mathrm{m}_1 \approx 0.068\ \mathrm{m}_0$, $\mathrm{m}_2 \approx 0.0734\mathrm{m}_0$ and $\mathrm{m}_3 \approx 0.084\ \mathrm{m}_0$ (m_0 is the free electron mass) and $\epsilon_{1,\mathbf{k}=0} \approx 13$ meV, $\epsilon_{2,\mathbf{k}=0} \approx 51$ meV and $\epsilon_{3,\mathbf{k}=0} \approx 109$ meV.

Before focusing on the laser properties, we examine the collision contributions and determine effective scattering and dephasing times for the presented structure.

3.2.4 Microscopic treatment of scattering

3.2.4.1 Population relaxation

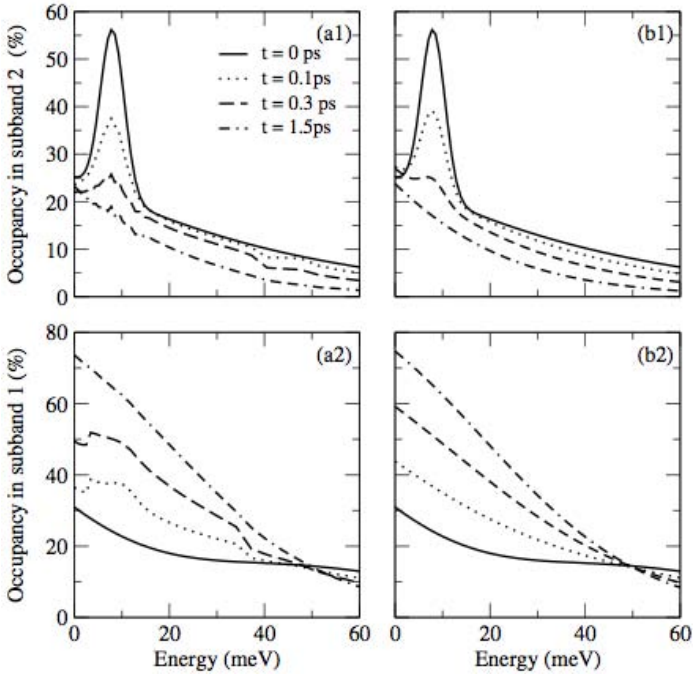

Figure 3.7. (Left column) Results of microscopic calculation for relaxation of carrier populations in subbands 2 (a1) and 1 (a2). (Right column) Corresponding results using the rate equation approximation.

We begin with a non-equilibrium carrier distribution in subbands 2 and 1 and investigate the relaxation of these distributions by solving the kinetic equations. Figure 3.7(a) shows the time evolution of the carrier distributions in the upper (a1) and lower (a2) subbands. With time, carrier-carrier and carrier-phonon collisions redistribute the carriers within each subband (intrasubband scattering) and between the subbands (intersubband scattering). The kinetic equation calculations indicate that the scattering between the two lowest subbands is strongly dominated by carrier-phonon interaction, as the energy spacing is almost completely equivalent to the (LO)-phonon energy. Next, we describe the scattering processes by the relaxation rate approximation. The results presented in Fig. 3.7(b) were obtained by approximating the collision

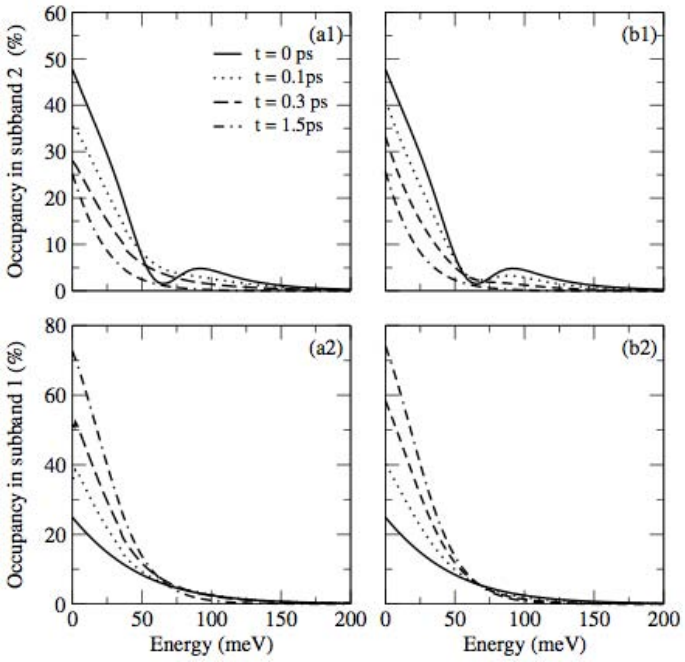

Figure 3.8. (Left column) Results of microscopic calculation for relaxation of carrier populations in subbands 2 (a1) and 1 (a2) for different initial conditions. (Right column) Corresponding results using the rate equation approximation with the same effective rates as in Fig. 3.7.

contributions between the two subbands according to

$$\begin{aligned} n_{1,\mathbf{k}}|_{\text{scatt,cc/cp}} &\approx -\gamma_{12}(n_{1,\mathbf{k}} - f_{1,\mathbf{k}}(\mu_{12}, T_l)) \\ &\quad -\gamma_{1,cp}(n_{1,\mathbf{k}} - f_{1,\mathbf{k}}(\mu_{l,1}, T_l)) - \gamma_{1,cc}(n_{1,\mathbf{k}} - f_{1,\mathbf{k}}(\mu_{pl,1}, T_{pl,1})) \quad (3.36) \\ n_{2,\mathbf{k}}|_{\text{scatt,cc/cp}} &\approx -\gamma_{12}(n_{2,\mathbf{k}} - f_{2,\mathbf{k}}(\mu_{12}, T_l)) \\ &\quad -\gamma_{2,cp}(n_{2,\mathbf{k}} - f_{2,\mathbf{k}}(\mu_{l,2}, T_l)) - \gamma_{2,cc}(n_{2,\mathbf{k}} - f_{2,\mathbf{k}}(\mu_{pl,2}, T_{pl,2})) \quad (3.37) \end{aligned}$$

with $\gamma_{12} = 3.3$ ps^{-1} ($\tau_{12} = 0.3ps$), $\gamma_{1,cp} = \gamma_{2,cp} = 0.5$ ps^{-1} ($\tau_{1,cp} = \tau_{2,cp} = 2ps$) and $\gamma_{1,cc} = \gamma_{2,cc} = 2$ ps^{-1} ($\tau_{1,cc} = \tau_{2,cc} = 0.5ps$). A comparison of the temporal development of the full calculation and the effective rate approximation shows good agreement, even though the initial distribution deviates strongly from quasi-equilibrium.

To demonstrate the general use of the obtained result, we show in Fig. 3.8 the relaxation for another set of initial conditions. Here, subband 2 has a dip above the optical phonon energy. For the effective rate approximation we use the same effective rates as in Fig. 3.7(b). Again, a comparison of the temporal development of the full calculation and the effective rate approximation shows good agreement.

Note that in contrast to the intrasubband scattering rates, $\gamma_{i,cp}$ and $\gamma_{i,cc}$, denoting carrier-phonon and carrier-carrier scattering rates, respectively, γ_{23} denotes a combined carrier-carrier and carrier-phonon rate. For our cases, carrier-carrier intersubband scattering always takes place on the same or on a longer time-scale than carrier-phonon scattering. Thus, intersubband scattering is here either dominated by carrier-phonon scattering or carrier-carrier and carrier-phonon scattering contribute equally. In the first case, carrier-carrier intersubband scattering can be neglected, while in the second case carrier-carrier and carrier-phonon scattering occur on the same time-scale. In both cases, the electrons relax to a Fermi-Dirac distribution at lattice temperature.

Similarly, we simulate the relaxation from non-equilibrium carrier distributions in subbands 3 and 2 using:

$$\begin{aligned} n_{2,\mathbf{k}}|_{\text{scatt,cc/cp}} &\approx -\gamma_{23}(n_{2,\mathbf{k}} - f_{2,\mathbf{k}}(\mu_{23}, T_l)) \\ &\quad -\gamma_{2,cp}(n_{2,\mathbf{k}} - f_{2,\mathbf{k}}(\mu_{l,2}, T_l)) - \gamma_{2,cc}(n_{2,\mathbf{k}} - f_{2,\mathbf{k}}(\mu_{pl,2}, T_{pl,2})) \quad (3.38) \\ n_{3,\mathbf{k}}|_{\text{scatt,cc/cp}} &\approx -\gamma_{23}(n_{3,\mathbf{k}} - f_{3,\mathbf{k}}(\mu_{23}, T_l)) \\ &\quad -\gamma_{3,cp}(n_{3,\mathbf{k}} - f_{3,\mathbf{k}}(\mu_{l,3}, T_l)) - \gamma_{3,cc}(n_{3,\mathbf{k}} - f_{3,\mathbf{k}}(\mu_{pl,3}, T_{pl,3})) \quad (3.39) \end{aligned}$$

The best agreement is achieved for:$\gamma_{23} = 0.9$ ps^{-1} ($\tau_{23} = 1.1ps$), $\gamma_{2,cp} = \gamma_{3,cp} = 0.5$ ps^{-1} ($\tau_{2,cp} = \tau_{3,cp} = 2ps$) and $\gamma_{2,cc} = \gamma_{3,cc} = 2$ ps^{-1} ($\tau_{2,cp} = \tau_{3,cp} = 0.5ps$).

Based on these investigations involving 2 subbands, we approximate the collision contributions in the 3-subband intersubband laser (cf. Eq. (3.29)) as follows:

$$\begin{aligned} n_{1,\mathbf{k}}|_{\text{scatt,cc/cp}} &\approx -\gamma_{12}(n_{1,\mathbf{k}} - f_{1,\mathbf{k}}(\mu_{12}, T_l)) - \gamma_{123}(n_{1,\mathbf{k}} - f_{1,\mathbf{k}}(\mu_{123}, T_l)) \\ &\quad -\gamma_{1,cp}(n_{1,\mathbf{k}} - f_{1,\mathbf{k}}(\mu_{l,1}, T_l)) - \gamma_{1,cc}(n_{1,\mathbf{k}} - f_{1,\mathbf{k}}(\mu_{pl,1}, T_{pl,1})) \quad (3.40) \\ n_{2,\mathbf{k}}|_{\text{scatt,cc/cp}} &\approx -\gamma_{12}(n_{2,\mathbf{k}} - f_{2,\mathbf{k}}(\mu_{12}, T_l)) - \gamma_{123}(n_{2,\mathbf{k}} - f_{2,\mathbf{k}}(\mu_{123}, T_l)) \\ &\quad -\gamma_{2,cp}(n_{2,\mathbf{k}} - f_{2,\mathbf{k}}(\mu_{l,2}, T_l)) - \gamma_{2,cc}(n_{2,\mathbf{k}} - f_{2,\mathbf{k}}(\mu_{pl,2}, T_{pl,2})) \quad (3.41) \\ n_{3,\mathbf{k}}|_{\text{scatt,cc/cp}} &\approx -\gamma_{123}(n_{3,\mathbf{k}} - f^3_{\mathbf{k}}(\mu_{123}, T_l)) \\ &\quad -\gamma_{3,cp}(n_{3,\mathbf{k}} - f_{3,\mathbf{k}}(\mu_{l,3}, T_l)) - \gamma_{3,cc}(n_{3,\mathbf{k}} - f_{3,\mathbf{k}}(\mu_{pl,3}, T_{pl,3})) \quad (3.42) \end{aligned}$$

with $\gamma_{12} = 2.5$ ps^{-1}, $\gamma_{2,cp} = \gamma_{3,cp} = 0.5$ ps^{-1} and $\gamma_{2,cc} = \gamma_{3,cc} = 2$ ps^{-1}. As the scattering rate between subband 2 and subband 3, γ_{23}, is distinctively smaller than the scattering rate between subband 1 and subband 2, γ_{12}, it is reasonable to assume that a quasi-equilibrium situation between subband 1 and subband 2 is reached long before subband 2 and subband 3 are in quasi-equilibrium. Consequently, for scattering between subband 2 and subband 3, the corresponding Fermi-Dirac distribution is the quasi-equilibrium distribution of all three subbands ($\gamma_{123} \approx \gamma_{23} = 0.9$ ps^{-1}).

3.2.4.2 Polarization

The effective rate for the damping of the polarization is determined on the basis of the linewidth of the absorption spectrum. In the microscopic calculations, it is crucial to include both diagonal and non-diagonal collision contributions [32, 37]. As shown in Fig. 3.9(b), the cancellation effects between diagonal and non-diagonal scattering contributions reduce the dephasing of the intersubband coherence enormously. Including diagonal scattering contributions only [cf. Fig. 3.9(a)], the spectrum is strongly homogeneously broadened, the lineshape being almost exactly Lorentzian. Non-diagonal scattering contributions counteract the diagonal ones and yield a reduced broadening of the spectrum. Due to non-diagonal contributions, the absorption is enhanced at the absorption peak. Furthermore, the absorption decreases much faster with detuning and does not form the long tail of a Lorentzian. Although, the non-diagonal contributions do yield not only a smaller linewidth, but also a reshaping of the spectrum, in all cases we have studied so far, the reducing of the broadening is the dominant impact. For this reason, we approximate the dephasing of the intersubband coherence [cf. Eq. (3.26)] with

$$\frac{d}{dt} p_{\mathbf{k}}^{23}|_{\text{scatt,cc/cp}} \approx -\gamma_p p_{\mathbf{k}}^{23} \tag{3.43}$$

where γ_p denotes an effective dephasing rate which is determined via the full absorption spectrum (here: $\gamma_p = 1.125$ ps^{-1}). A comparison of the absorption spectrum with kinetic equations and with the spectrum obtained in rate approximation shows almost complete agreement on a logarithmic scale, where on the linear scale the lineshapes differ slightly. The result of the full calculation is slightly more symmetric in shape than the result obtained with the rate approximation due to the reshaping influence of the non-diagonal contributions which is neglected in the rate approximation. However, the main impact of the non-diagonal contributions, namely the reducing of the broadening due to the diagonal contributions, can be reproduced very well with the effective dephasing rate.

3.2.5 Laser Simulations

3.2.5.1 Temperature dependence of laser intensity: influence of many-body contributions and bandstructure

As first application of the theory, we investigate the temperature dependence of the laser intensity-current density relation shown in Fig. 3.10. In order to describe the scattering processes in the laser, we investigate the absorption spectrum and the relaxation from given non-equilibrium carrier distributions as described in Sec. 3.2.4 - for the different lattice temperatures of interest. Although the investigated non-equilibrium distributions will most likely differ from the non-equilibrium distributions in the laser, the response of the system depends stronger on the system parameters such as lattice temperature and carrier wave functions than on the shape of the non-

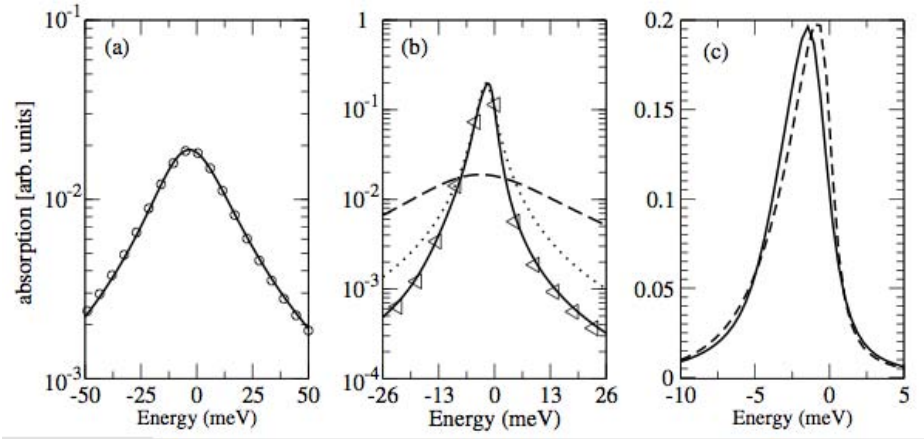

Figure 3.9. (a) Considering only the diagonal scattering contributions (solid line) yields a strongly broadened absorption spectrum, almost identical with a Lorentzian fit (circles). (b) Non-diagonal scattering contributions reduce broadening. The full calculation (solid line) yields a spectrum less broadened than the spectrum neglecting the non-diagonal contributions (dashed line). A comparison with a Lorentzian fit (dotted line) illustrates clearly the non-lorentzian shape. Approximating scattering in effective rate approximation (triangles) yields a very good agreement on the logarithmic scale. (c) A comparison of full calculation (solid line) and rate approximation (dashed line) on linear scale shows small differences in lineshape.

equilibrium carrier distributions. For this reason, we regard the set of scattering rates as system parameters which depend on lattice temperature and carrier wave functions and determine the rates with the use of typical non-equilibrium carrier distributions. The same set of scattering rates is then used in all calculations involving the same lattice temperature.

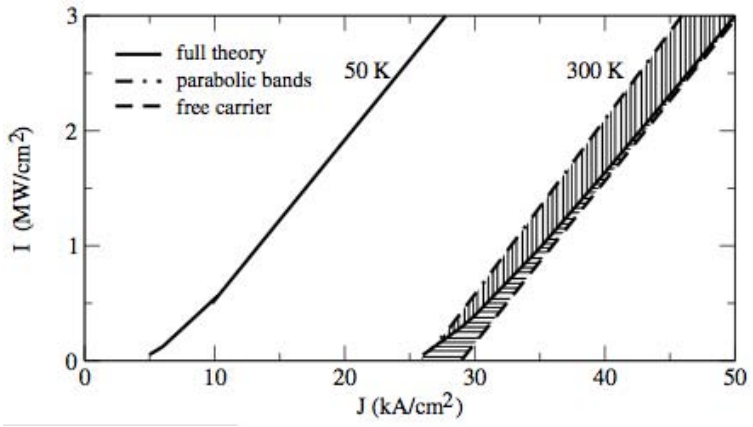

Figure 3.10. Laser intensity-current density relation for laser A at temperatures $T = 50$ K and $T = 300$ K. The laser intensity increases with increasing current density. Note the high threshold current density for the highly doped laser at $T = 300$ K. Lasers B and C have lower threshold current densities: $J_{th}^{B}(300) \approx 16.5$ kA/cm^2 and $J_{th}^{C}(300) \approx 1.6$ kA/cm^2 (not shown).

The observed temperature dependence is strongest for a laser with a high carrier density and less pronounced for a laser with a lower carrier density. The difference in threshold current density is reduced from $J_{th}^{A}(300) - J_{th}^{A}(50) \approx 23$ kA/cm^2 for $n_e^A = 1 \times 10^{12}$ cm^{-2} (cf. Fig. 3.10) to $J_{th}^{B}(300) - J_{th}^{B}(50) \approx 15.6$ kA/cm^2 for $n_e^B = 6 \times 10^{11}$ cm^{-2} (not shown) to only $J_{th}^{C}(300) - J_{th}^{C}(50) \approx 1.45$ kA/cm^2 for $n_e^C = 5 \times 10^{10}$ cm^{-2} (not shown). This dependence of the threshold current density on temperature and carrier density is due to temperature and density dependent band-filling effects. The difference in the population of the subbands according to the quasi-equilibrium distribution of the system is dependent on temperature and density. For example, the quasi-equilibrium distribution of the system at $T = 300$ K locates 2.5% of the carriers in subband 3 for carrier density n_e^C an increased number of 3.2% for carrier density n_e^B and finally 3.7% of the carriers for carrier density n_e^A. Thus, the scattering processes which drive the non-equilibrium carrier distributions of the laser towards the quasi-equilibrium distribution of the system yield an effective fill-up of subband 3 - strongest for the highly doped laser. A laser at lattice temperature $T = 50$ K where the quasi-equilibrium distribution of the system sees almost no carriers in subband 3 does not experience these relaxation-induced band-filling effects. For better comparison we express the density dependence of the laser in terms of the characteristic temperature

T_0 according to

$$J_{\text{th}}(T) = J_{\text{th}}(50)\text{e}^{\frac{T-50K}{T_0}} \ . \tag{3.44}$$

As can be seen in Fig. 3.11, the characteristic temperature reaches a minimum value for a laser with a moderate carrier density of $n_e = 4 \times 10^{11}$ cm^{-2}. The threshold current density increases steadily with increasing carrier density, which has also been reported in [42].

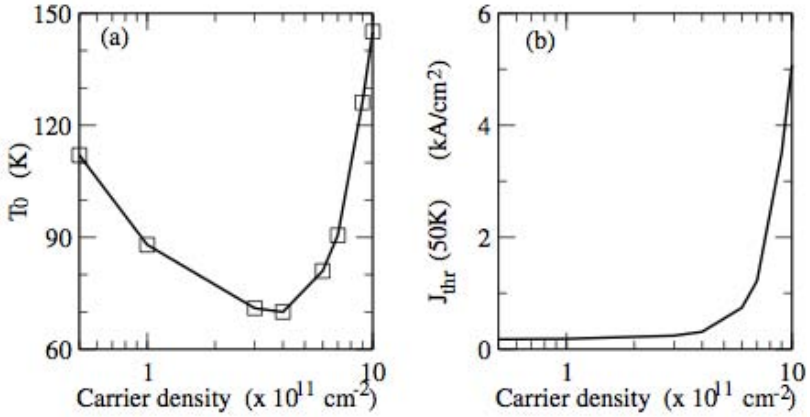

Figure 3.11. (a) Doping dependency of characteristic temperature (a) and threshold current density for T=50 K (b).

The obtained results are comparable to measured light output-to-current characteristics of quantum cascade lasers [cf. for example [38]]. However, all experimental investigations of the laser intensity-to-current density relation show a roll-over of the laser intensity with increasing current density. This roll-over is not observed by our model. This suggests, that the roll-over is due to extrinsic processes. Recently, Jovanovic et al. reported the calculated saturation of modal gain and saturation current density as a function of the carrier density. Note, that this saturation is not connected to the roll-over of the laser intensity as a function of the current density as the latter occurs for a fixed carrier density.

To investigate the impact of Hartree-Fock effects and inhomogeneous broadening, we compare the results of the full calculation with (1) a calculation neglecting the nonparabolicity of the conduction band (parabolic conduction band, dot-dashed line) and (2) a calculation neglecting Hartree-Fock effects (free carrier, dashed line).

3.2.5.2 Nonparabolicity Effects

The impact of inhomogeneous broadening due to the nonparabolicity of the conduction band can be seen for the laser at $T = 300$ K in Fig. 3.10: the solid line is the result

of the calculation where we considered the nonparabolicity of the conduction band according to Ekenberg, that is the energy dispersion of the subbands is considered in the effective mass approximation with different effective masses for the subbands. Compared to other systems (e.g. InAs/AlSb quantum wells) the nonparabolicity of the conduction band in AlGaAs/GaAs quantum wells is relatively small. For this reason, the energy dispersion of the conduction band of AlGaAs/GaAs quantum wells is often approximated by a parabola yielding energy subbands with identical curvature and transition energies independent of the wave vector **k**:

$$\tilde{\epsilon}_{32,\mathbf{k}} = \frac{\hbar k^2}{2}(\frac{1}{m_3} - \frac{1}{m_2}) \tag{3.45}$$

with $m_2 = m_3 = 0.0665\, m_0$ (dot-dashed line) instead of $m_2 = 0.0735624 m_0$, $m_3 = 0.083747\ m_0$ (solid line). Already the relatively small nonparabolicity of the AlGaAs/GaAs quantum well yields a decrease in the overall laser intensity. Assuming a parabolic conduction band, the slope of the laser intensity to current density relation is much steeper.

3.2.5.3 Hartree-Fock effects

The importance of many-body effects on intersubband transitions in single quantum wells in the linear regime is well established and their influence on intersubband absorption/gain spectra has been investigated both experimentally and theoretically [39]-[41]. Recently, Pereira et al. investigated in [26] the impact of Hartree-Fock effects on absorption and gain in a characteristic QCL structure and found rather small impact on the gain and stronger impact on the absorption region. The influence of the Hartree potential on the effective bandstructure in a QCL structure has been examined in [42]. Here, we take into account the renormalizations of (a) band structure and (b) Rabi frequency and determine the impact of these Hartree-Fock effects on the laser intensity to current density relation for a laser at lattice temperature $T = 300K$. In Fig. 3.10, we compare a full calculation (solid line) with a calculation neglecting Hartree-Fock effects (dashed line). As can be seen, the inclusion of Hartree-Fock effects yield a small reduction of the laser intensity. The effect is strongest close to threshold current density and diminishes for higher current densities. The exchange contribution,

$$\epsilon_{\mathbf{k}}^{HF,I}(t) = \sum_{\mathbf{q}} \sum_{a=1}^{3} n_{a,\mathbf{q}}(t)[V_{\mathbf{k}-\mathbf{q}}^{3aa3} - V_{\mathbf{k}-\mathbf{q}}^{a22a}] \tag{3.46}$$

renormalizes the transition energy between the two laser subbands. Equation 3.46 shows that this renormalization depends on the Coulomb matrix elements and the carrier distributions in the subbands and is thus dependent on both wave-vector **k** and time. Generally, the change in transition energy is strongest for $\mathbf{k} = 0$ and increases with increasing current density. The reason for the increase with current

density can be found in the different population numbers. As the shift in transition energy is dependent on the **k**-dependent occupation number, an increase in current density, which yields an increase in the population numbers of the laser subbands, yields stronger shifts in transition energy. Similar, the excitonic contribution and the depolarization effect yield time and wave vector dependent renormalizations of the Rabi frequency:

$$\Omega_{\mathbf{k}}|_{HF,II}(t) = -\frac{1}{\hbar}\sum_{\mathbf{q}} V^{3232}_{\mathbf{k}-\mathbf{q}} p^{23}_{\mathbf{q}}(t)\,, \quad \Omega_{\mathbf{k}}|_{HF,III}(t) = \frac{2}{\hbar} V^{3223}_{0} \sum_{\mathbf{q}} p^{23}_{\mathbf{q}}(t)\,. \tag{3.47}$$

Whereas the depolarization effect has no wave-vector dependence, the counteracting excitonic contribution is strongest for small **k**. For $\mathbf{k} = 0$, the excitonic contribution dominates, yielding a slightly enhanced Rabi frequency, whereas for larger **k** the depolarization effects dominates, yielding a slightly reduced Rabi frequency. Note, that the Hartree-Fock contributions introduce also an imaginary part of the Rabi frequency. However, the renormalizations of transition energy and Rabi frequency are relatively small, compared to the original transition energy and the original Rabi frequency. Although, the impact of the Hartree-Fock contributions increases with increasing current density, the increase of the original Rabi frequency is stronger, yielding a reduction of the already small impact of the Hartree-Fock renormalizations.

3.2.5.4 Modulation Response

In this section, we illustrate the capability of our theory to describe the dynamical response of an intersubband laser. We modulate the injection current of the laser after it has reached steady-state conditions by replacing γ in Eq. (3.25) with

$$\gamma_{mod}(t) \;=\; \gamma\{\Theta(t_1 - t)(1 - \mathrm{e}^{-a(t_1)}) + \Theta(t - t_2)(1 - \mathrm{e}^{-a(t_2)})\}\,. \tag{3.48}$$

[cp. Fig. 3.12(a)]. In Figure 3.12, we present the dynamical response of laser A (see previous section) at two different lattice temperatures $T_1 = 50$ K and $T_2 = 300$ K, respectively. In the following, we refer to laser A operated at temperature $T = 50$ K as laser A_{50}, at $T = 300$ K as laser A_{300}. Figure 3.12(b) indicates that after steady-state operation is achieved, the laser intensity reaction is time-delayed with respect to the modulation of the injection current, with the time-delay being temperature dependent.

At time $t = 0$, both lasers are in steady-state operation with a laser intensity of ≈ 0.38 MW/cm^2. Whereas the injection current is in both cases reduced to the minimal value in ≈ 1.6 ps, it takes considerably longer until the laser intensities of both lasers vanished. The laser intensity of laser A_{50} vanishes after ≈ 4.5 ps. In the first 1.5 ps of its decay, the laser intensity decreases with almost the same rate as the injection current, but time-delayed by ≈ 0.6 ps. In the next 0.7 ps, the laser intensity

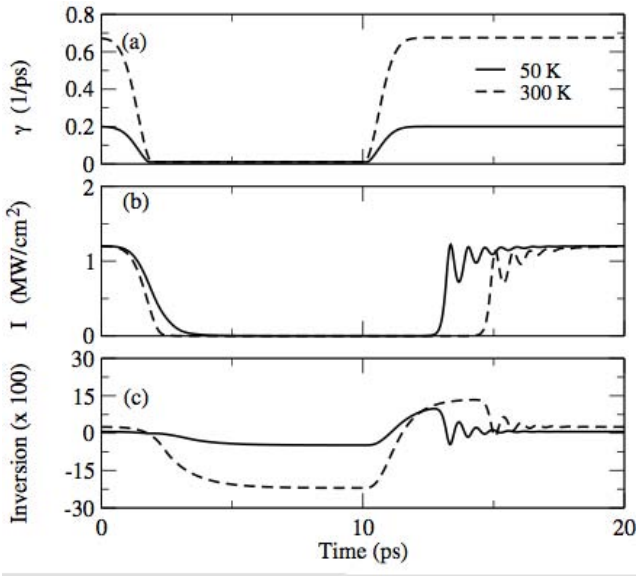

Figure 3.12. Injection current modulation (a) and laser response involving (b) laser intensity and (c) population inversion (enlarged by a factor of 100) for laser at lattice temperatures $T = 50, 300$ K.

decreases slower than the injection current and continues decreasing after the injection current has been cut off for already 0.6 ps. In contrast to this, laser A_{300} reacts faster to the change in injection current. Time-delayed by only ≈ 0.3 ps, the laser intensity vanishes almost the whole time with roughly the same turn-off time as the injection current. Due to the decreasing injection current, in both cases the population in the upper laser subband is reduced, yielding a decrease of the inversion between the two laser subbands [cp. Fig. 3.12(c)]. Fig. 3.13 shows the change in the population in the three subbands for both lasers. Under steady-state conditions, the total number of carriers is divided as follows: laser A_{50}: 87% of the carriers are in subband 1, 6% in subband 2 and 7% in subband 3; laser A_{300}: 51% of the carriers are in subband 1, 23% in subband 2 and 26% in subband 3. The cut-off of the injection current yields a strong decrease in the populations of subband 3 and an almost equivalent increase in the populations of subband 1 for laser A_{50}. In laser A_{300} the increase in subband 1 is smaller than the decrease in subband 3. This difference goes together with a stronger change of the population in subband 2 than for laser A_{50}. Whereas for laser A_{50}, strong electron-phonon scattering between subband 3 and subband 2 effectively depletes subband 2 and fills subband 1, the same scattering processes are not equally efficient for laser A_{300}. Due to the higher lattice temperature of laser A_{300}, the quasi-equilibrium carrier distribution of this system already locates a substantial amount of carriers in subband 2.

Overall, the change in the populations in subband 2 has only a small impact on the

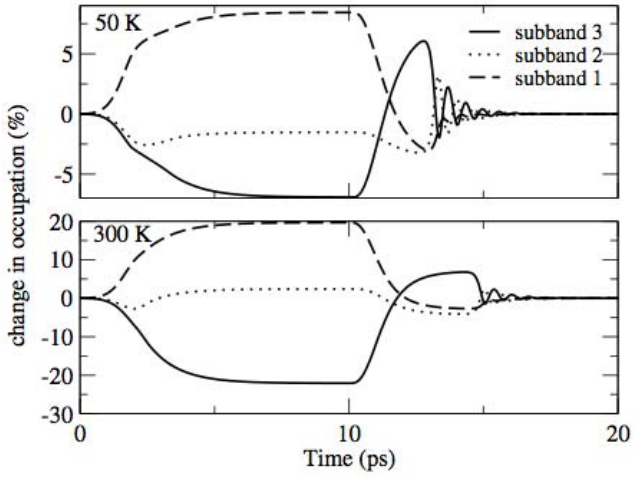

Figure 3.13. Change in the population in the three subbands as response to the modulation of the injection current.

inversion [cf. Fig. 3.12(c)] as it is considerably smaller than the change in populations in subband 3. The changes in population are considerably bigger for laser A_{300}. As this laser has a higher threshold current density, a higher current density is required to pump the laser into a steady-state operation with the same laser intensity as for laser A_{50}. Consequently, the steady-state populations are distinctively different for both lasers and a modulation in injection current has a stronger impact on the populations in laser A_{300}.

At $t \approx 1.2$ ps the inversion vanishes for laser A_{50} and the active medium switches to absorption. The switch from gain to absorption of laser A_{300} follows 0.2 ps later. At $t \approx 10.3$ ps, the injection current is increased again. The populations of the upper laser subband are increased and around $t \approx 11.$ ps the inversion reappears for the laser at 50 K. In the presence of laser gain, the laser field now builds up. Lasing at 300 K reappears slightly later, at $t \approx 11.5$ ps. This time delay is again due to the difference in the quasi-equilibrium carrier distributions for the two lasers. The population in subband 3 has to be considerably larger for laser A_{300} than for laser A_{50} in order to achieve inversion. After $t \approx 13.3$ ps, the injection current remains constant, having reached its starting value again. Stimulated emission and scattering processes lead now to a decrease in the population of subband 3, which is no longer compensated by an increase in injection current, and relaxation oscillations can be observed before the laser returns to steady-state operation. A comparison of the relaxation oscillation frequencies of the two laser shows that the relaxation oscillation frequency is almost temperature independent with $f_{A_{50}} = 1510$ GHz and $f_{A_{300}} = 1550$ GHz. These high relaxation oscillation frequencies arise from the fast time scales of carrier and photon decay which are on the order of *ps*.

Finally, we present in Fig. 3.14 the response of the frequency shift of the laser field

to the modulation of the injection current. Here, the laser at low lattice temperature shows stronger frequency shifts than the laser at high lattice temperature. The frequency shift can vary by up to 70 GHz for laser A, but only 10 GHz for laser A_{300}.

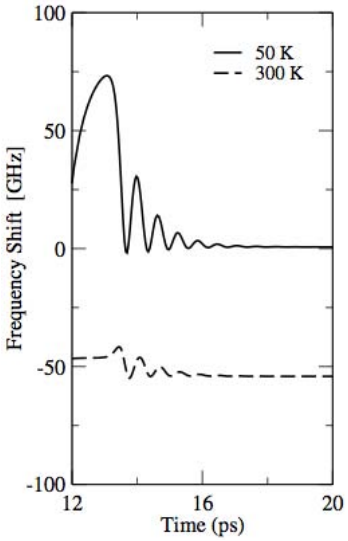

Figure 3.14. Change in phase as the laser switches back to steady-state operation. To allow a better comparison, the trace for the laser operation at 300 K was moved by 1.7 ps, so that both lasers have laser intensity of $\approx 0.2\text{MW/cm}^2$ at $t = 14$ ps.

3.3 Conclusion

In summary, we have presented two theoretical models for the description of steady-state and dynamical properties of conventional (direct) intersubband lasers. In section 3.1, we presented a theoretical model for the prediction of steady-state characteristics which self-self-consistently calculates the bandprofile (with respect to bandbending effects) and the steady-state non-equilibrium carrier distribution of direct QCLs. The implementation of this model increases Sandia's in-house design capabilities by allowing access to a more advanced predictive laser model than originally present.

In section 3.2, we presented a theoretical model for the investigation of dynamical laser properties. The theory considers the nonlinear interaction between the laser field and active medium of intersubband lasers by simultaneously solving Maxwell's equations for the laser field and the semiconductor Bloch equations for the gain medium. In addition to first order many-body contributions (Hartree-Fock), second order many-body contributions (scattering) are taken into account by connecting the laser theory

to a microscopic treatment of carrier-carrier and carrier-phonon scattering. As examples for possible applications of the dynamic theory, we discussed the laser intensity to current density relation and the reaction of laser intensity and subband population to current modulation for a three-subband intersubband laser.

Chapter 4

A new type of QCL: optically pumped electrically driven THz QCL

As the strong temperature dependence of conventional THz QCLs appears to be intrinsic, i.e. the strong reduction of population inversion with increasing temperature which limits the present maximum operation temperature to 164 K [10], the pursuit of conceptually new approaches for THZ QCLs is obvious. Optical conversion is one approach to generate THz radiation which simultaneously reduces the problem of both, parasitic current channels and thermal backfilling. It offers the possibility to a) locate the lasing subbands energetically high enough to prevent thermal backfilling and b) to decrease the amount of parasitic current channels due to a reduced coupling between the lasing and the surrounding subbands. Instead of electrical pumping, optical pumping is used to populate the upper laser subband and THz radiation is obtained either via stimulated emission or by exploiting electron Raman scattering (e.g., [43],[44] or recently [45]). However, while conventional optical conversion presents a solution to the problem of population thermalization, it also introduces a fundamental constraint due to the Manley-Rowe quantum limit. The highest achievable conversion efficiency is given by the quotient of output and input frequencies, i.e. for FIR to THz conversion this translates into a maximum conversion efficiency of $\approx 10\% - 15\%$. Additionally, optical conversion schemes based on second order nonlinear mixing (e.g. [46],[47],[48]) have the disadvantage of phase-matching constraints.

For this reason, we investigated the feasibility of an optically-pumped electrically-driven quantum cascade laser, which is schematically shown in Fig. 4.1. The original thought leading to the design of this laser was to develop a way to optically inject electrons into the upper states of a lasing transition and maintain population inversion at high temperatures, while overcoming the Manley-Rowe efficiency limit (maximum of 1 THz photon per pump photon absorbed) by using a dc electric field for the THz power source. The logic behind this postulation are:

1. By placing the long wavelength optical transition high in the structure leakage current is eliminated as carriers in the left most well have difficulty tunneling across the next two wells. This will significantly lower leakage current, thereby

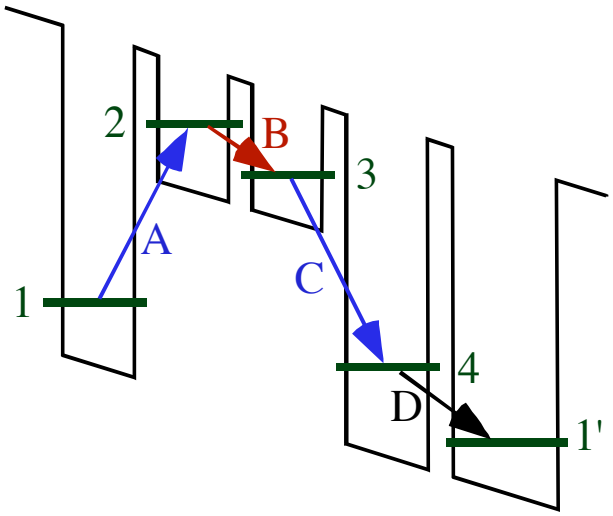

Figure 4.1. Basic Principle of Optically Assisted Electrically Pumped Lasing.

reducing power consumption and resistive heating while improving efficiency.

2. By optically pumping from the left well (injector well) into the next well (transition A) very selective pumping into the upper state of the long wavelength transition (transition B) is achieved.

3. Since a dc electric field is applied to the structure, It is possible to engineer transition C to have the same energy as transition A. Thus the optical pump can stimulate the downward transition (transition C) from the lower state of the long wavelength transition, serving both to depopulate the lower lasing level as well as to recycle the pump photons, and minimize excess heating resulting from LO phonon emission or other non-radiative depopulation channels of the lower lasing level.

4. The applied dc field also allows one to engineer the energy levels so that 1' is lower than 4. Then LO phonons (transition D) can then be used to return the electrons to the "injector" well of the next period. The more phonons are used the better the optical recycling efficiency should be (at the expense of more electrical power input).

5. By this process, the optical pump can be used for selective injection into the upper state, rapid depopulation of the lower state, and population inversion control, while the additional dc electrical power applied supplies the energy for the long wavelength photons as well as the optical phonons, allowing the pump photons to be recycled.

In contrast to optical conversion schemes, the THz energy is not derived from the external optical field, but comes from the forward electrical bias as in a conventional

QCL. In this way our approach is similar to recently proposed designs for THz generation using Bloch oscillations in superlattices [49, 50]. However, in contrast to [49, 50], our design allows the coherent recovery of the pump field. Therefore, we get the advantages of an optical conversion scheme, but circumvent the constraint of the Manley-Rowe limit.

Furthermore, as we will see below, the proposed scheme not only generates THz radiation via stimulated emission as we hoped, but also from automatically phase-matched quantum coherence contributions. Besides potentially enabling THz generation at room temperature, the quantum coherence generated in these structures enables new types of non-linear optics. Until very recently, quantum optical phenomenon (such as lasing without inversion and electrically induced transparency) had been restricted to atomic systems. Recently, an experiment has shown gain without inversion in semiconductors but based on the same principles as atomic systems. We will see below that the ability to add a DC electric field to semiconductor systems, adds features not obtainable with atomic systems enabling engineering control of quantum coherence not presently available.

4.1 Theoretical Background

In the following, we demonstrate the capabilities of the scheme to generate THz radiation theoretically by investigating the intensities of the involved optical fields, i.e. the THz field and the pump field, using Maxwell's wave equations:

$$\frac{d}{dt}\mathcal{H}(r,t) = -\frac{1}{\mu}\nabla \times \mathcal{E}(r,t) \tag{4.1}$$

$$\frac{d}{dt}\mathcal{E}(r,t) = \frac{1}{\epsilon}\nabla \times \mathcal{H}(r,t) - \frac{1}{\epsilon}\frac{d}{dt}\mathcal{P}(r,t) \tag{4.2}$$

In Eq. 4.1, $\mathcal{E}(r,t) = \sum_i \mathcal{E}_i(r,t)$ ($\mathcal{H}(r,t) = \sum_i \mathcal{H}_i(r,t)$) denotes the total electric (magnetic) field, consisting of THz (i =THz) and pump (i =P) field. The material response has been divided into a nonresonant part, lumped in with the (background) refractive index n, and a resonant part, treated dynamically in terms of the macroscopic optical polarization $\mathcal{P}_i(r,t)$. The latter is composed of the respective microscopic polarizations P_{ab} between subbands a and b

$$\mathcal{P}_{\mathrm{THz}} = (d_{14}\,P_{14} + d_{23}\,P_{32}) + c.c.\,, \tag{4.3}$$

$$\mathcal{P}_{\mathrm{P}} = (d_{12}\,P_{21} + d_{34}\,P_{34}) + c.c.\,, \tag{4.4}$$

which are calculated within the framework of the semiconductor Bloch equations:

$$\begin{aligned}\frac{d}{dt}P_{ab} &= (\frac{\mathrm{i}}{\hbar}E_{ab}-\gamma)P_{ab}+\frac{\mathrm{i}}{\hbar}d_{ab}(n_a-n_b)(\mathcal{E}_{\mathrm{THz}}+\mathcal{E}_{\mathrm{P}}) \\ &\quad +\frac{\mathrm{i}}{\hbar}\sum_{\substack{c=1\\c\neq a,b}}^{c=4}(d_{bc}P_{ac}-d_{ac}P_{cb})(\mathcal{E}_{\mathrm{THz}}+\mathcal{E}_{\mathrm{P}}) \qquad (4.5)\\ \frac{d}{dt}n_a &= \frac{\mathrm{i}}{2\hbar}\sum_{\substack{c=1\\c\neq a}}^{c=4}d_{ca}(P_{ca}-P_{ac})(\mathcal{E}_{\mathrm{THz}}+\mathcal{E}_{\mathrm{P}})+\frac{d}{dt}n_a|_{\mathrm{s}}\,. \qquad (4.6)\end{aligned}$$

d_{ab} is the dipole moment and E_{ab} the transition energy between subbands a and b, determined self-consistently within a Schrödinger-Poisson solver. n_a denotes the population of subband a, γ the dephasing rate of the polarizations and $\frac{d}{dt}n_a|_{\mathrm{s}}$ accounts for population relaxation effects due to carrier-carrier and carrier-phonon scattering. These contributions are taken into account with microscopically determined scattering rates (for details see e.g. [51]). Equation 4.5 shows the dependence of the polarizations on two distinct contributions: I. stimulated emission or absorption (population dynamics) and II. quantum coherence effects (microscopic polarization interference). Quantum coherence effects, caused by quantum interference of different channels of radiative processes, were first observed in atomic systems. In our system, the influence on the THz field from polarizations induced by dipole-forbidden transitions ($1 \leftrightarrow 3$ and $2 \leftrightarrow 4$), offers the possibility of absorption cancellation without emission cancellation. As a result, effects such electromagnetically induced transparency (EIT) and lasing without inversion (LWI) can be observed (for a textbook discussion see e.g. [52]). We will show in the following discussion, that both stimulated emission and quantum coherence contributions can give rise to a substantial amount of THz radiation in the proposed QCL.

4.2 Theoretical Results

We evaluate the general capabilities of the proposed scheme for the example of an AlGaAs/GaAs structure with a sheet carrier density of $N = 3\times10^{11}$ cm^{-2}, operated at a lattice temperature of $T = 220$ K. The relevant transition energies, dipole moments and lifetimes are calculated as: $E_{21} = E_{34} = 144$ meV, $E_{23} = 16$ meV, $d_{12} = d_{34} = 1.5$ nm, $d_{23} = 4$ nm, $\tau_{21} = 4.4$ ps, $\tau_{23} = 1.2$ ps, and $\tau_{34} = 5.7$ ps. From our quantum kinetic calculations we determine the dephasing rate for the THz transition as $\gamma = 2.5$ ps^{-1} which agrees with the experimental results presented in [53]. The total loss consisting of contributions from waveguide, mirror and free carrier absorption is estimated to be $\alpha_{THz} = 140$ cm^{-1} for the THz field and $\alpha_{FIR} = 50$ cm^{-1} for the pump field.

4.2.1 Benefits of pump recycling

First, we investigate the benefits of the coherent recycling of the pump. Therefore we simulate the response of the structure to optical excitation with a Gaussian pulse (temporal width σ=30 ps, peak pump intensity I_{PP} = 16.5 MW/cm^2) which spatially propagates perpendicular to the growth direction, i.e. the pulse propagates in the quantum-well-in-plane direction x. In Fig. 4.3, we present the time and space dependence of optical pump and generated THz field for a system with pump recovery, in Fig. 4.4 the corresponding data for a system without pump recovery. A direct comparison of the depletion of the pump field and the resulting buildup of THz radiation with (solid lines) and without (dashed lines) pump recycling [see Fig. 4.2], shows that pump recycling yields a strongly increased propagation length, resulting in an enhanced gain of THz radiation. As a figure of merit for the general feasibility of the scheme and the benefits of the pump recycling, we investigate the optical conversion efficiency η which is the ratio of maximum output over input (i.e. THz pulse energy over pump pulse energy for pulse excitation and THz intensity over pump intensity for cw excitation, respectively). For the example presented in Fig. 4.2, with recycling we achieve an optical conversion efficiency of η = 10.3 %, while without recovery of the pump energy we achieve an optical conversion efficiency of only η = 2 %. Thus, recycling the pump energy increases the optical conversion efficiency for this example by a factor of 5.

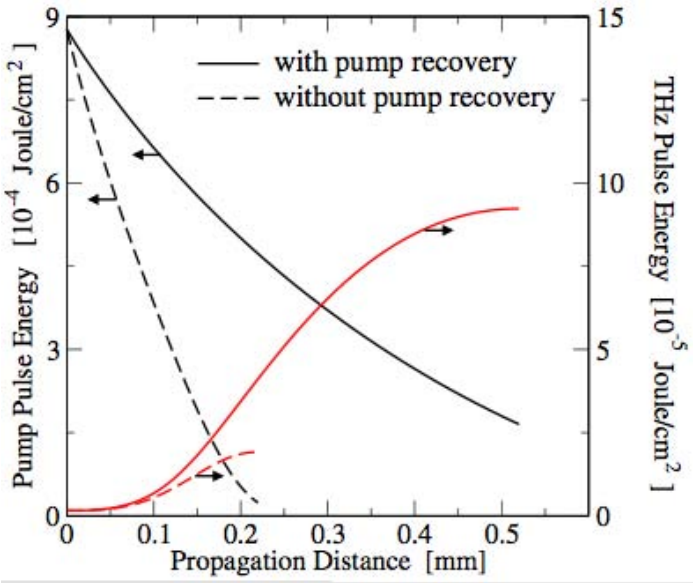

Figure 4.2. Spatial response (at 220 K) to pulse excitation propagating in the quantum-well-in-plane direction for a design with pump recycling (solid lines) and without pump recycling (dashed lines). A 5 times enhanced conversion efficiency is achieved from coherent pump recovery.

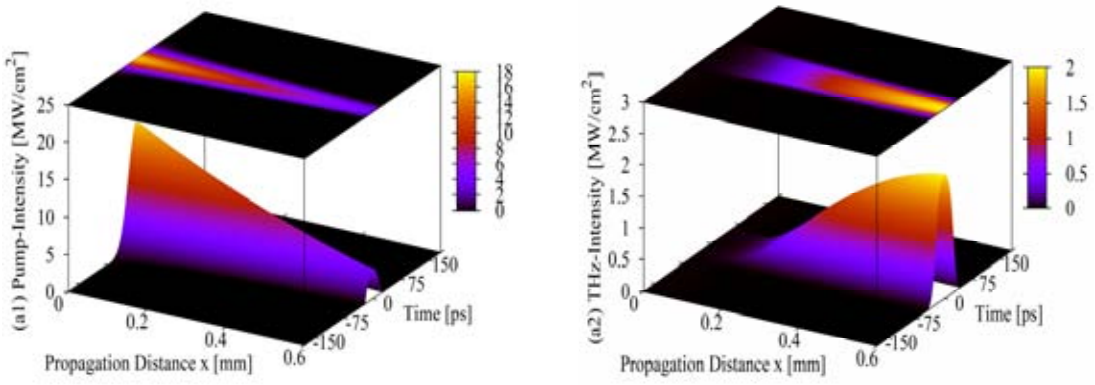

Figure 4.3. Time and space dependence of optical pump (a1) and THz radiation (a2) propagating in the quantum-well-in-plane direction for a design *with pump recycling*.

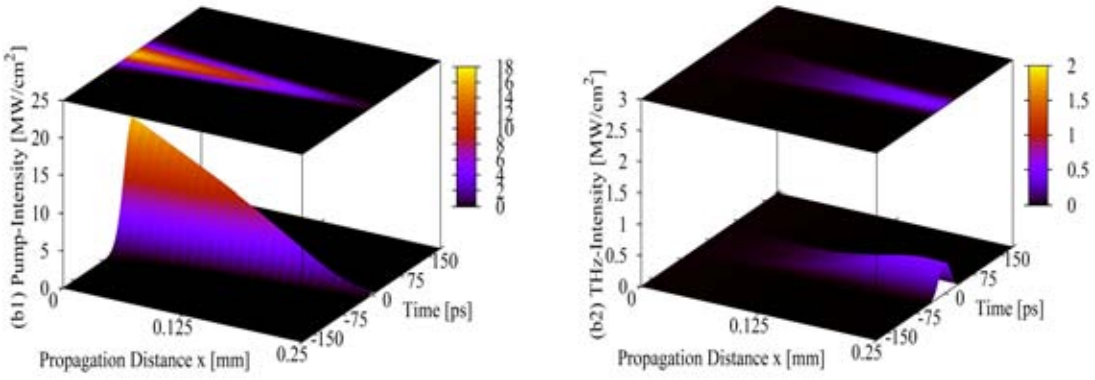

Figure 4.4. Time and space dependence of optical pump (a1) and THz radiation (a2) propagating in the quantum-well-in-plane direction for a design *without pump recycling*. Notice the shorter propagation length, yielding a drastically reduced buildup of THz radiation.

4.2.2 Influence of excitation strength and duration

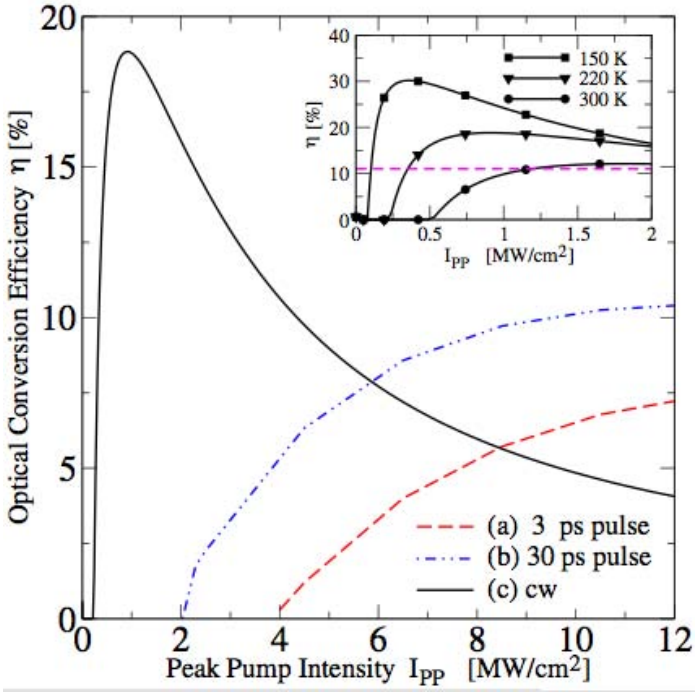

Figure 4.5. Dependence of optical conversion efficiency on peak pump intensity I_{PP} at 220 K for (a) excitation with a 3 ps pulse, (b) excitation with a 30 ps pulse and (c) continuous-wave excitation. The inset shows the temperature dependence of the optical conversion efficiency for cw excitation, demonstrating the possibility to exceed the Manley-Rowe limit (dashed line).

Next, we examine the dependence of the optical conversion efficiency on the pump energy for (a) excitation with a 3 ps pulse, (b) excitation with a 30 ps pulse and (c) continuous-wave excitation (cf. Fig. 4.5). A comparison of the predicted conversion efficiencies shows a strong dependence on the excitation duration. As the generation of THz radiation is not only due to stimulated emission, but also to quantum coherence contributions, i.e. interference of generated polarizations, the buildup of THz radiation can increase with increasing excitation duration. The highest optical conversion efficiencies are observed for cw-excitation. For completeness, we present in the inset of Fig. 4.5 the (cw) optical conversion efficiencies for operation at different lattice temperatures, $T = 150, 220$, and $300K$, all of which are higher than the highest operational temperature achieved for (cw) THz-QCLs to date.

We find that for weak excitation, the optical conversion efficiency increases with increasing peak pump intensity. However, for higher peak pump intensities the THz

gain slowly saturates due to a combination of both optical Stark effect and pump-induced population redistribution (similar to the saturation predicted for optically-pumped semiconductor quantum wells in [54]). As a result, the optical conversion efficiency is maximized for an optimal pump intensity which can be clearly seen for the example of cw-operation in Fig. 4.5.

Due to temperature dependent non-radiative carrier recombination and dephasing of the polarizations, the highest achievable optical conversion efficiency and the width of the window for optimal pump intensity are also temperature dependent (cf. inset of Fig. 4.5) yielding a decrease of optical conversion efficiency with increasing temperature. However, even for room temperature operation our approach predicts promising optical conversion efficiencies.

4.2.3 Small signal gain

In Fig. 4.6, we present the dependence of the amplitude modal THz gain on the detuning of a weak THz-probe field from the lasing transition, $\delta_\omega = \hbar\omega_{THz} - (E_2 - E_3)$. Table 4.1 gives an overview over the corresponding pump intensities and relative populations of the various subbands for the considered cases pictured in Fig. 4.6. For excitation with a small cw-pump field (case A), population inversion between the lasing subbands is not obtained and there is only absorption. However, with increasing pump intensity, we observe the onset of quantum coherence effects: electromagnetically induced transparency (EIT) and then lasing without inversion (LWI) in cases B and C, respectively. Numerical simulations showed no phase-matching requirement. We confirm this result analytically by solving the Bloch equations for resonant continuous-wave (cw) excitation and negligible resonant THz-probe field. Expressing the polarization of the THz transition solely in terms of the steady-state populations of subbands $1-4$ gives:

$$Im(P_{32}) = \Big[\frac{(n_2 - n_3)\gamma}{2(|\tilde{\Omega}_P|^2 + \gamma^2)} + \frac{|\tilde{\Omega}_P|^2(n_1 + n_2 - n_3 - n_4))}{8\gamma(|\tilde{\Omega}_P|^2 + \gamma^2)}\Big]\tilde{\Omega}_{\mathrm{THz}}\,. \tag{4.7}$$

In Eq. 4.7, γ denotes the dephasing time of the intersubband coherences, $n1-n4$ the steady-state populations of subbands $1-4$ (which depend on the intensity of the pump field) and $\tilde{\Omega}_{\mathrm{i}} = \hbar^{-1} d_{\mathrm{i}} \tilde{\mathcal{E}}_{\mathrm{i}}$ the Rabi frequency of field $\tilde{\mathcal{E}}_i$. Note that for simplicity, we here give only the explicit result for the special case of an optically-pumped electrically-driven QCL with $d_{12} \equiv d_{34} = d_{\mathrm{P}}$.

The first term in Eq. 4.7 accounts for the possible generation of THz radiation via stimulated emission, thus this contribution only yields THz gain if there is a population inversion. The second term in Eq. 4.7 accounts for quantum coherence contributions and can give rise to THz gain whenever the subband populations fulfill the condition $n_1 + n_2 - n_3 - n_4 > 0$, which allows lasing without population inversion.

	I_P [MW/cm^2]	$\frac{n_1}{N}$	$\frac{n_2}{N}$	$\frac{n_3}{N}$	$\frac{n_4}{N}$
A	0.006	0.93	0.026	0.041	0.003
B	0.098	0.63	0.162	0.189	0.019
C	0.151	0.582	0.194	0.198	0.026
D	0.631	0.479	0.301	0.167	0.053

Table 4.1. Pump intensity and relative steady-state populations of subbands $1-4$ for cases A-D of Fig. 4.6.

For the design presented in Fig. 1, all sources of THz radiation in Eq. 4.7 depend on the pump field only through its intensity and are consequently automatically phase-matched to the THz field. For cases *A*-*C* of Fig. 4.6, population inversion between the lasing subbands (subband 2 and subband 3) does not exist, thus, the observed gain is due to the second term in Eq. 4.7, i.e. quantum coherence contributions. Finally, in case *D*, population inversion is obtained and stimulated emission also contributes to the THz gain. However, the necessary population condition for the quantum coherence contributions is fulfilled as well. Thus, both stimulated emission and quantum coherence simultaneously contribute to the THz gain. Evaluating Eq. 4.7 for the parameters of case *D* shows, that at zero detuning both mechanisms contribute roughly equally to the THz gain. The inset of Fig. 4.6, shows the dependence of the maximum amplitude modal gain on the pump intensity. With increasing pump intensity, the gradual saturation of the pump-induced population redistribution and the onset of the optical Stark effect yield a saturation of the modal gain.

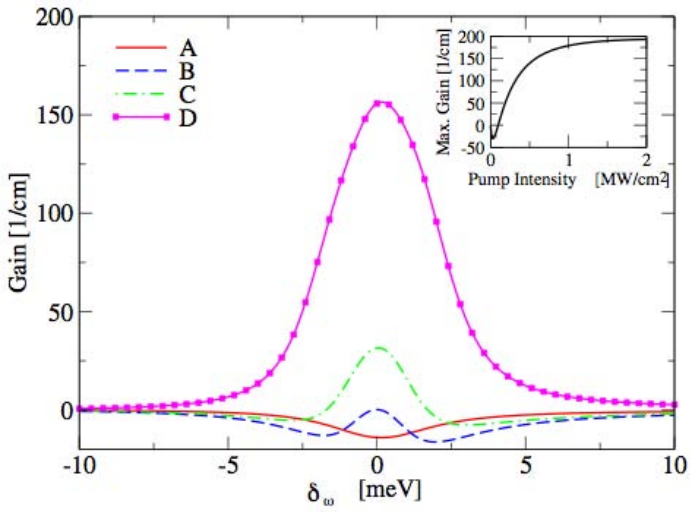

Figure 4.6. Amplitude modal gain (half of intensity gain) at 220 K as function of THz-probe detuning and pump intensity.

4.2.4 Influence of extrinsic scattering mechanisms

Recently, interface roughness has been identified as an important extrinsic scattering mechanism. However, the influence of interface roughness on lifetimes and dephasing rates depends crucially on the sample of interest. In order to estimate the dependence of the approach on the quality of the sample, i.e. on extrinsic scattering such as interface roughness, we present in Figs. 4.7 and 4.8 the influence of extrinsic scattering mechanisms on the small-signal gain.

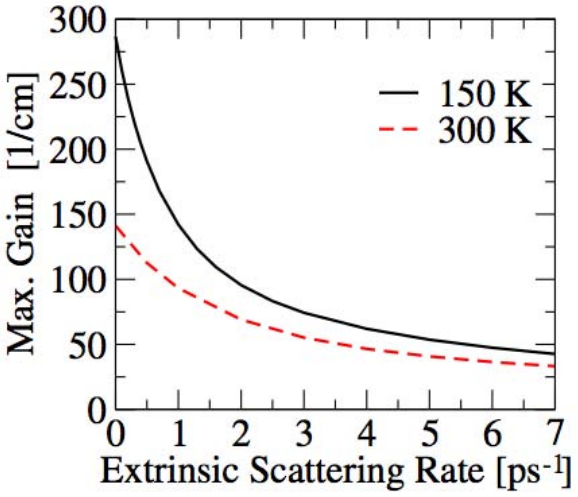

Figure 4.7. Dependence of maximum modal small-signal gain (for resonant pump and probe field) on extrinsic scattering rate γ_{ext} with $\gamma_{tot} = \gamma_{int} + \gamma_{ext}$ for operation at 150 K and 300 K. The intrinsic rates, γ_{int}, due to carrier-carrier and carrier-phonon scattering are extracted from quantum-kinetic calculations and are given in the text.

Figure 4.7 shows the maximum gain for resonant pump and resonant probe excitation over extrinsic scattering rate γ_{ext} for operation at 150 K and 300 K. Low temperature operation generally yields a stronger gain than high temperature operation, however, with increasing extrinsic scattering rates, the temperature dependence of the gain decreases.

In order to deepen our understanding of the influence of γ_{ext} on the performance of the scheme, we investigate in Fig. 4.8 (A) the dependence of the small-signal gain on the pump intensity for the examples of $\gamma_{ext} = 0.5\text{ps}^{-1}, 2\text{ps}^{-1}$, and 5ps^{-1}. Except for very low pump intensities (here below ≈ 0.1 MW/cm^2), the gain always decreases with increasing γ_{ext}, as does its dependence on the pump intensity. Figure 4.8 (B) shows the corresponding population difference between the lasing subbands. The presented data illustrates that an increase in γ_{ext} requires an increase in pump

intensity to achieve a certain amount of population inversion. Whereas for example, external excitation with a pump intensity of 1 MW/cm^2 yields population inversion of ≈ 0.08 for $\gamma_{ext} = 0.5$ ps^{-1}, the same excitation yields population inversion of only ≈ 0.02 and ≈ 0.0012 for $\gamma_{ext} = 2$ ps^{-1} and $\gamma_{ext} = 5$ ps^{-1}, respectively. The observed dependence of the ratio of population inversion over pump intensity on γ_{ext} appears to be an obvious reason for the decrease of gain with increase of γ_{eff} [as it can be seen in Fig. 4.8 (A)]. However, a comparison of the gain as a function of population inversion [see Fig. 4.8 (C)], shows that this dependence is not the only reason for the reduced gain. Comparing the ratios of gain over population inversion for different γ_{ext}, we find that with increasing γ_{ext} the same population inversion yields a decreasing amount of gain. This decrease is due to gain cross-saturation, i.e. quantum coherence contributions which yield saturation or decrease of gain due to the increase in pump intensity. Thus while the population inversion is the same, which one would expect to yield the same amount of gain, the total gain differs due to the quantum coherence dependence on the pump intensity.

In summary, the decrease of gain with increasing γ_{ext} has two origins: 1. the decreased ratio of population inversion over pump intensity (the same pump yields smaller population inversion) and 2. the decreased ratio of gain to population inversion (the same population inversion yields smaller gain due to stronger pump intensity). Note, that Fig. 4.8 (C) also shows another feature of quantum coherence effects: gain without inversion. This feature can be observed most clearly for small γ_{ext}, where gain is generated although the lower laser subband is populated more strongly than the upper one. However, when both laser subbands are populated equally, the observed gain is almost independent of γ_{ext}.

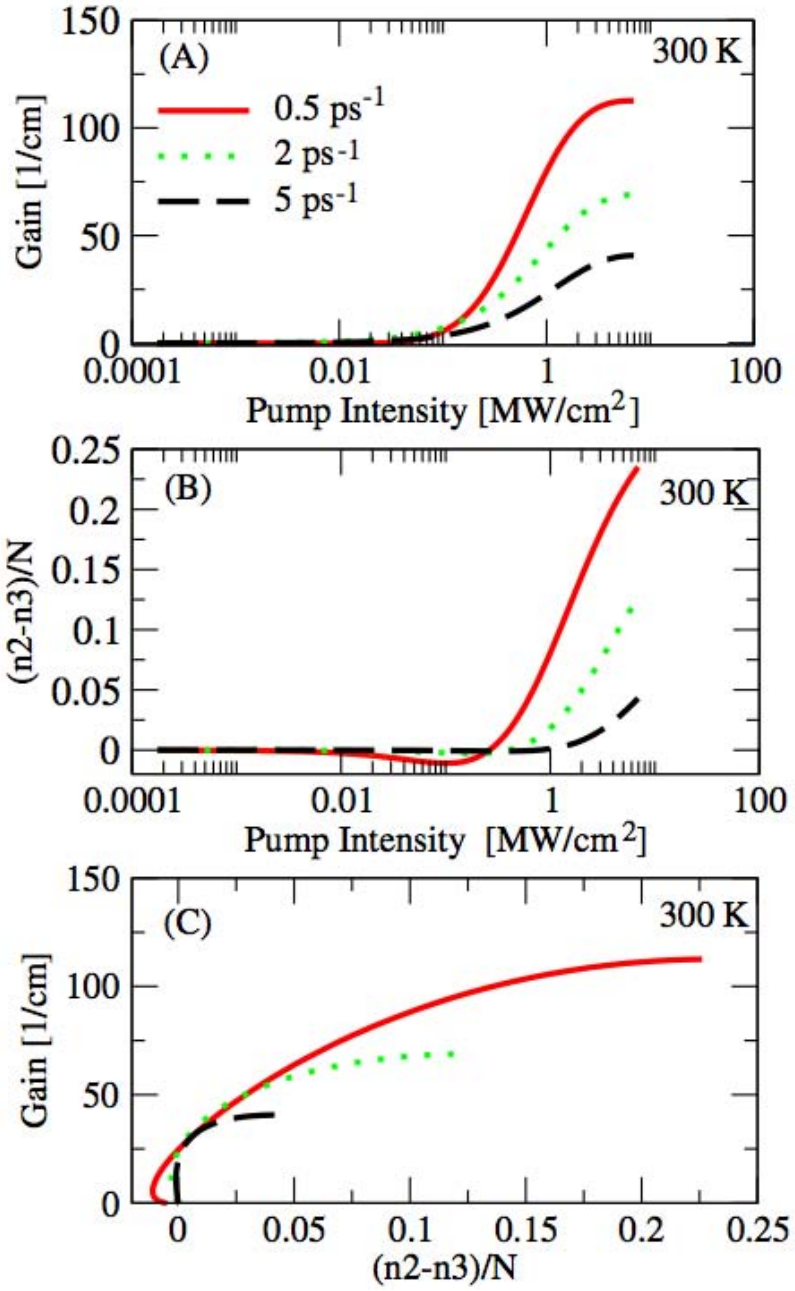

Figure 4.8. A) Dependence of small-signal gain on pump intensity for three different extrinsic scattering rates, (B) dependence of the relative population difference on pump intensity, and (C) corresponding gain plotted as a function of population difference. Note that quantum coherence effects allow the generation of gain without population inversion between the lasing subbands.

4.3 Conclusion

In conclusion, we have investigated the optically-pumped electrically-driven quantum cascade laser as a conceptually new approach for THz QCL. Theoretical investigations showed promising optical conversion efficiencies for both pulsed and cw-excitation for a broad temperature range up to 300 K. The predicted efficiencies can dramatically exceed the Manley-Rowe quantum limit due to coherent recycling of the pump field. For weak excitation the optical conversion efficiency increases with increasing peak pump intensity, while for strong excitation the optical conversion efficiency decreases due to a saturation of the modal gain leaving a temperature-dependent window for optimal pump excitation. Calculated gain spectra demonstrated that both stimulated emission and automatically phase-matched quantum coherence contributions can give rise to THz radiation. As a result, the approach is not only a promising source for THz generation at high temperatures, but also an interesting model system for investigating quantum coherence effects such as electromagnetically induced transparency and lasing without inversion, and the potential to go beyond mimicking atomic quantum coherence systems by exploiting the extra engineering knobs enabled by the addition of an applied dc electric field.

Chapter 5

Frequency-Shift Quantum-Cascade Laser Designs and Simulations

5.1 Introduction

Tunable terahertz (THz) quantum-cascade lasers (QCL) are a prerequisite of a compact and robust QCL-base spectrometer, which can be used for molecular sensing applications. Currently, several tuning schemes have been demonstrated such as external cavity [55], temperature [56], current [57], distributed feedback (DFB) period [58, 59], cleave length [60], and very recently scaled thickness [61, 62]. All of these techniques with the exception of the last, do not alter the gain curve (the finite frequency region controlled by the laser design over which the laser can operate) but only shift the output frequency within the gain curve limits and are only useful over limited frequency scans.

The last method (scaling the laser thickness) falls into a separate category. It is not designed to scan a specific laser around a central frequency, but to be able to generate separate lasers each with a gain curve centered on a different frequency. This is essential for creating lasers that have a gain curve that overlaps the frequency of absorption lines of molecules one wishes to detect.

The line of reasoning of the scaled thickness method is that, since the design of a THz QCL for a specific frequency is not trivial, it is more convenient to modify a known design by adjusting the well and barrier by the same fractional amount. Doing so does change the lasing frequency, but it does not guarantee the preservation of the characteristics of the original laser since the wavefunctions, the anticrossing, and coupling splitting energies are not kept to the original shapes and values.

The work presented below is similar to the scaled thickness method in that our goal was to base our QCL design on a proven working design and modify the structures such that they lase at different specified frequencies. Our method, however, is significantly different from the scaled thickness method since, besides changing the lasing frequency, we also would like the new structure to inherit the characteristic and performance of the original structure as well. In order to achieve these goals, instead of blindly altering the thickness of each well and barrier by the same fractional amount,

we developed a computer routine that automatically modifies the thickness of each layer such that the wavefunctions, the anticrossing and coupling splitting energies are kept unchanged while only changing the energy of the lasing transition.

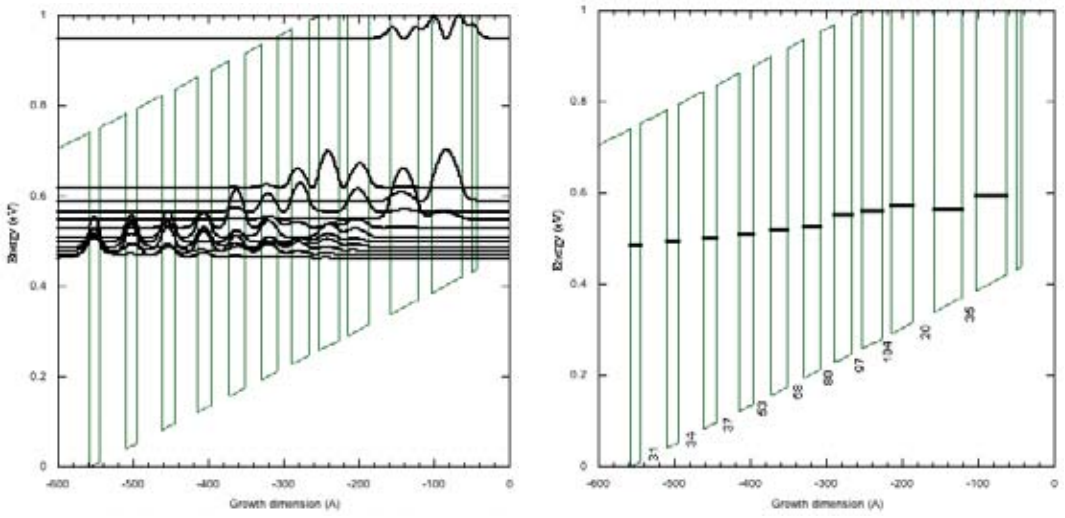

(a) **(b)**

Figure 5.1. (a) Example potential profile (green) and magnitude of the corresponding wavefunctions (black) (b) The relative energy levels calculated for each well in isolation (black) and the anticrossing energy (numbers) for the two wells separated by the barrier numbered.

The basic algorithm can be described as follows. First we start with a known laser bandstructure. For example see Fig. 5.1(a). Here we can see the potential profile (in green) and the magnitude of the corresponding wavefunctions. The laser emits in the MIR for the example shown when electrons transition from the highest state to the third highest state. If we want to change the laser frequency, the width of the well containing the optical transition (second from the right) must be changed. This will not only change the energy separation between the two states, but also the absolute energy of the lower state. Thus to keep relative alignment of the lowest state with the other states around it, every well and barrier will need to be altered. In order to do this we first analyze the structure to determine two metrics: (i) what is the relative energy difference for the ground state in each well compared to the lowest lasing level, and (ii) how strongly are these states coupled to each other. To first order the first is determined by the width of each well and the electric field applied, and the second is mostly determined by the width of the barrier separating each pair of wells. To calculate the relative energy levels the eigenenergies of each well are computed with the well in isolation and this energy is corrected by the potential drop between the well and the lowest lasing level due to the electric field. For the example bandstructure shown in Fig. 5.1(a), the energy of the isolated wells is plotted as straight lines in Fig.

5.1(b). The second is determined by taking two wells at a time with the appropriate barrier between them, adjusting the electric field until the energy level in each well (if they were isolated) is lined up with each other, and calcuting the energy separation between the resulting two "anti-crossed states". Due to the finite coupling between the states, two states will appear with one above the aligned isolated energy level and one below it. The amount of separation represents the strength of the coupling (the narrower the barrier, the stronger the coupling, the bigger the energy separation). This energy separation when the isolated energy levels are aligned is the anticrossing energy - for the case shown in Fig. 5.1(b) the anticrossing energy is given below each barrier. Both of these numbers are not completely accurate when all the wells are considered together, but they are physically important and well defined making them good candidates to use to automate designs.

To create a new design we just need to modify the well with the lasing transition to give the energy we want and then recreate the rest of the structure based off of the relative energy levels and coupling strengths, modifying the electric field strength as required until we create a structure with nearly identical characteristics except for the lasing energy. The actual algorithm currently employed makes a small deviation from the above description, but the principle is still the same. The change is that the isolated energies are not used to reassemble the structure, but the energy levels in pairs of wells are used instead. The result is essentially the same, but the implementation is slightly different. The details of this process are described below.

5.2 Newton's (or Simplex) Method

We already have a computer program to analyze a given QCL structure, which determines the values of the anticrossing and coupling splitting energies between all the adjacent wells throughout a QCL structure. Based on the Newton's or simplex method, we developed an optimization program, which, for a given set of anticrossing and coupling splitting energy values, can generate a corresponding QCL structure. In this section we will first examine the one dimension (1-D) Newton's method and the more generalized three dimension (3-D) Newton's method. Finally, the application of the Newton's method to the generation of a QCL structure will be presented.

5.2.1 1-D Newton's Method

The 1-D Newton's method is a way to numerically solve $f(x) = 0$ for x. By letting x_o be our guess and ε_o be the error, we can write $x = x_o + \varepsilon_o$. From Taylor's series expansion and we have:

$$f(x_o + \varepsilon_o) = f(x_o) + \varepsilon_o f'(x_o) + \frac{\varepsilon_o^2}{2} f''(x_o) + ... \tag{5.1}$$

We then can approximate $f(x)$ by ignoring the higher order term:

$$f(x_o + \varepsilon_o) \approx f(x_o) + \varepsilon_o f'(x_o) \tag{5.2}$$

$$\varepsilon_o = -\frac{f(x_o)}{f'(x_o)} \tag{5.3}$$

where x_o now is our initial guess and ε_o is the error of the initial guess. By correcting our initial guess by the initial error, we arrive at a new guess, $x_1 = x_o + \varepsilon_o$, which is closer to the solution, and the new error term ε_1. The process above is repeated with the error term becomes smaller and smaller until x is found.

5.2.2 3-D Newton's Method

The 3-D Newton's method is slightly more complicate, since the goal now is to determine a solution (x, y, z) to a set of equations $F(x, y, z) = G(x, y, z) = H(x, y, z) = 0$. Eq. (5.3) can be rewritten in a 3-D matrix form as:

$$\begin{bmatrix} F_x & F_y & F_z \\ G_x & G_y & G_z \\ H_x & H_y & H_z \end{bmatrix} \begin{bmatrix} \varepsilon_x \\ \varepsilon_y \\ \varepsilon_z \end{bmatrix} = \begin{bmatrix} -F(x_o, y_o, z_o) \\ -G(x_o, y_o, z_o) \\ -H(x_o, y_o, z_o) \end{bmatrix} \tag{5.4}$$

where

$$\begin{aligned} F_x &= \left.\frac{\partial F}{\partial x}\right|_{x_o}, \quad F_y = \left.\frac{\partial F}{\partial y}\right|_{y_o}, \quad F_z = \left.\frac{\partial F}{\partial z}\right|_{z_o} \\ G_x &= \left.\frac{\partial G}{\partial x}\right|_{x_o}, \quad G_y = \left.\frac{\partial G}{\partial y}\right|_{y_o}, \quad G_z = \left.\frac{\partial G}{\partial z}\right|_{z_o} \\ H_x &= \left.\frac{\partial H}{\partial x}\right|_{x_o}, \quad H_y = \left.\frac{\partial H}{\partial y}\right|_{y_o}, \quad H_z = \left.\frac{\partial H}{\partial z}\right|_{z_o} \end{aligned} \tag{5.5}$$

The error terms for x, y, and z can be expressed as:

$$\varepsilon_x = \frac{\begin{vmatrix} -F & F_y & F_z \\ -G & G_y & G_z \\ -H & H_y & H_z \end{vmatrix}}{D}, \varepsilon_y = \frac{\begin{vmatrix} F_x & -F & F_z \\ G_x & -G & G_z \\ H_x & -H & H_z \end{vmatrix}}{D}, \varepsilon_z = \frac{\begin{vmatrix} F_x & F_y & -F \\ G_x & G_y & -G \\ H_x & H_y & -H \end{vmatrix}}{D} \tag{5.6}$$

where D is the determinant

$$D = \begin{vmatrix} F_x & F_y & F_z \\ G_x & G_y & G_z \\ H_x & H_y & H_z \end{vmatrix} \tag{5.7}$$

The new approximated solution is $(x_1, y_1, z_1) = (x_o + \varepsilon_x, y_o + \varepsilon_y, z_o + \varepsilon_z)$. The process is repeated until the solution is found.

5.2.3 Implementation

The objective of the optimization program is that for a giving initial well width, the program will determine the adjacent well width (w) and the thickness of the barrier (b) between them, which will result in the desired coupling splitting energy ($CSgoal$) and anticrossing splitting energy ($ASgoal$) - see App. A. The set of equations which we need to solve is:

$$CS(w,b) - CSgoal = AS(w,b) - ASgoal = 0 \tag{5.8}$$

or

$$\triangle cs(w,b) = \triangle as(w,b) = 0 \tag{5.9}$$

The 2-D version of Eq. (5.3) with an initial guess (w_o, b_o) can be expressed as:

$$\left[\begin{array}{cc} c_w & c_b \\ a_w & a_b \end{array} \right] \left[\begin{array}{c} \varepsilon_w \\ \varepsilon_b \end{array} \right] = \left[\begin{array}{c} -\triangle cs \\ -\triangle as \end{array} \right] \Bigg|_{w_o, b_o} \tag{5.10}$$

where the error terms and the matrix of the partial derivatives are

$$\varepsilon_w = \frac{c_b \triangle cs - a_b \triangle as}{c_w a_b - c_b a_w}, \varepsilon_b = \frac{a_w \triangle cs - c_w \triangle as}{c_w a_b - c_b a_w} \tag{5.11}$$

$$\begin{aligned} c_w &= \frac{\partial \triangle cs}{\partial w}\Bigg|_{w_o} = \frac{\triangle cs(w_o+0.0001) - \triangle cs(w_o-0.0001)}{0.0002} \\ c_b &= \frac{\partial \triangle cs}{\partial w}\Bigg|_{b_o} = \frac{\triangle cs(b_o+0.0001) - \triangle cs(b_o-0.0001)}{0.0002} \\ a_w &= \frac{\partial \triangle as}{\partial w}\Bigg|_{w_o} = \frac{\triangle as(w_o+0.0001) - \triangle as(w_o-0.0001)}{0.0002} \\ a_b &= \frac{\partial \triangle as}{\partial w}\Bigg|_{b_o} = \frac{\triangle as(b_o+0.0001) - \triangle as(b_o-0.0001)}{0.0002} \end{aligned} \tag{5.12}$$

A good initial guess for w_o and b_o is very important to ensure that the optimization program will "climb the correct hill" so that the final solution is not something unreasonable such as a negative well width or barrier thickness. To address this problem, we break our optimization program into two parts: (1) crude search, which will give us the initial guess, and (2) fine search, which utilizes the Newton's method. For crude search, we set the initial thickness of the barrier to 3 Å and the initial well width of the adjacent well to be the same as that of the first well. With applied electric field, this will make sure that the energy level associated with the adjacent well is below the energy level associated with the first well. The thickness of the barrier is then increased by 1 Å at a time until the anticrossing splitting energy is close to the desired value. This will give us b_o. After that, we decrease the well width by 1 Å at a time until the coupling splitting energy is close to the desired value, which provides us w_o. So far the initial guess found from the crude search have been satisfactory.

5.3 Results

5.3.1 Modelling results

We applied the optimization program based on the simplex method to a high performance 4-quantum well, THz QCL structure. The original structure that we chose was a demonstrated high performance laser designed at MIT (FL178C-M10 [63])and grown at Sandia. The latter is an important consideration since a given design frequently will perform quite differently when grown on another MBE machine. Using the routine we created many different frequencies, 4 of which were subsequently grown in order to verify the modeling. The time is takes for the computer to create each new frequency is on the order of 15 minutes, significantly reducing the typically 3-5 days to design a structure from scratch.

Some example results from the modeling are shown in Fig. 5.2 which illustrate some of the capabilities of the method. Recall that the primary goal was to generate structures that are essentially identical except for shifting the THz output frequency by changing the energy separation between the two lasing subbands in the structure. Comparing Figs. 5.2(b) and 5.2(c) to Fig. 5.2(a), one can immediately note that the wavefunctions in each structure are nearly identical to each other, while the energy separation between the two lasing subbands has clearly changed. While the wavefunction appearance is not precisely quantitative, the relative shapes have a strong effect on the parameters that are important such as the dipoles and scattering times between the states. By maintaining wavefunctions of roughly the same spatial extent, and the same energy separation and the same shapes, the dipoles and scattering rates remain very similar which is indeed the case for the two examples shown. Therefore the lasers should exhibit very similar performance but at different frequencies. Fig. 5.2(b) shows the bandstructure for a laser with the frequency shifted down by 0.8 THZ to 2.5 THz and the Fig. 5.2(c) shows the bandstructure for a laser with the frequency shifted up by 0.8 THz to 4.1 THz from the original design at 3.3 THz.

Figs. 5.2(d) and 5.2(e) give the bandstructure and the magnitude of the wavefunctions where we have scaled all the thicknesses of the layers uniformly by 10%, which is the only other method that has been tried in order to shift the frequency without redesigning from scratch. There are a couple of notable differences in these cases. First even though the frequencies were changed by a smaller amount from the original than the previous cases, the wavefunctions have noticeably changed shapes - particularly the 3 level (in green). For the case of 10% thicker layers, the coupling between the 3rd and 4th states is clearly reduced. This will lead to a slower emptying of the lower laser level, which will lower population inversion and reduce the laser performance. For the 10% thinner layers, the coupling is significantly enhanced and now their will be enhanced scattering between states 5 and 3 which can reduce the population in the upper lasing state with similar loss of performance. The loss in performance as the frequency scales has indeed been observed experimentally.

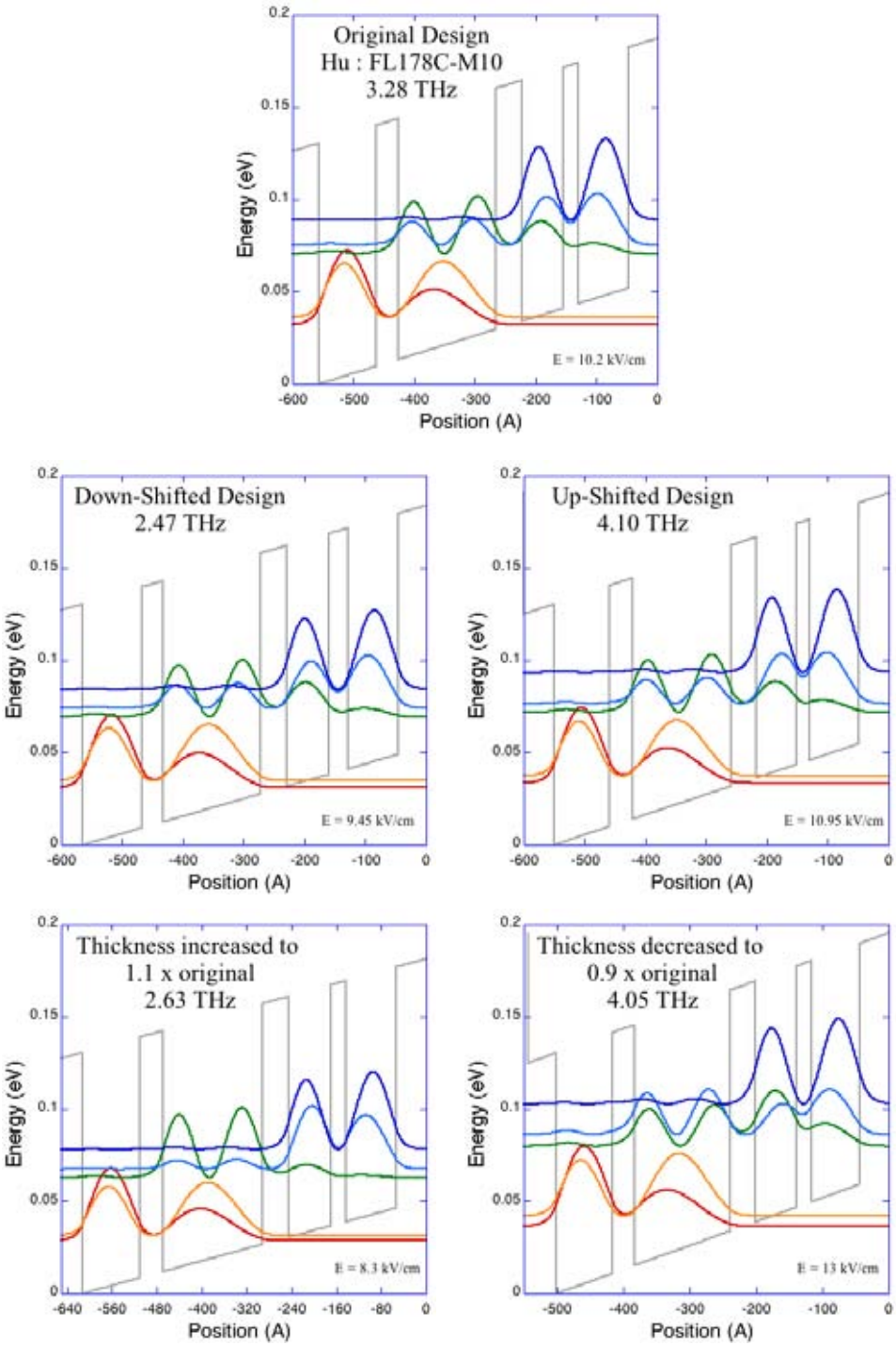

Figure 5.2. (a) Bandstructure of original structure to be shifted to other frequencies. The top two wavefunctions correspond to the lasing transition. (b) Frequency down-shifted and (c) up-shifted bandstructures created by keeping the anticrossing and coupling energies identical. (d) Frequency down-scaled and (e) up-scaled bandstructure resulting from scaling the thickness uniformly.

Other noticeable differences are the much larger change in the electric fields, different energies differences for all the states and not just the lasing states, and much different lengths of the structure. The first does not have a impact on the behavior of the laser, but the second and third influence many of the physical mechanisms for the laser operation.

5.3.2 Experimental Results

A few lasers have been grown to test out the shifting algorithm with design frequencies of 2.82, 3.05, 3.28 (the original design) and 3.75 THz. Fig. 5.3(a) and 5.3(b) show the spectra for the 3.28 and 3.75 THz designs. One can immediately observe that indeed the higher frequency design shifted operation to higher frequencies. Both lasers, however, emit light below the design frequency. This is actually a common characteristic of this particular type of laser design. Both are nearly 10% below the frequency they were designed for, but the scaling between the two frequencies agrees well with the scaling expected from the design shifts presented above (design 14% difference, experiment 17% difference). Typically the exact laser frequency will also depend on the cavity losses and threshold currents as the laser transitions will actually depend on electric field until threshold. Looking at the light-voltage versus current relations in Figs. 5.3(c) and 5.3(d), we note that the current is indeed quite a bit different. Some of the difference is accounted for by the 25% increase of the laser area for the 3.75 THz laser, but there is still roughly a factor of 2 higher current density. The best guess for this is that the higher frequency laser has higher doping, which increases the losses and therefore the current threshold. Since the laser is operating at a higher voltage it is also expected that the laser frequency will shift to higher frequencies.

Unfortunately, the material at 2.82 and 3.05 THz did not lase. The MBE facilities were disrupted early in the project and did not come back on-line until the last 6 months of the project. While certain quantifiable aspects of the material quality are still below the levels they were at before the capability was taken off-line, it cannot be said with certainty whether the lack of lasing was a result of a growth related issue, a design issue, or something unrelated to either. It can be said, however, that multiple regrowths of the 3.28 design have also yielded less than a 30% lasing rate since the MBE has been brought back on-line, so there is a good chance that the design is not the issue. Once the MBE machines are back to a steady reproducible state, this experiment should be tried again.

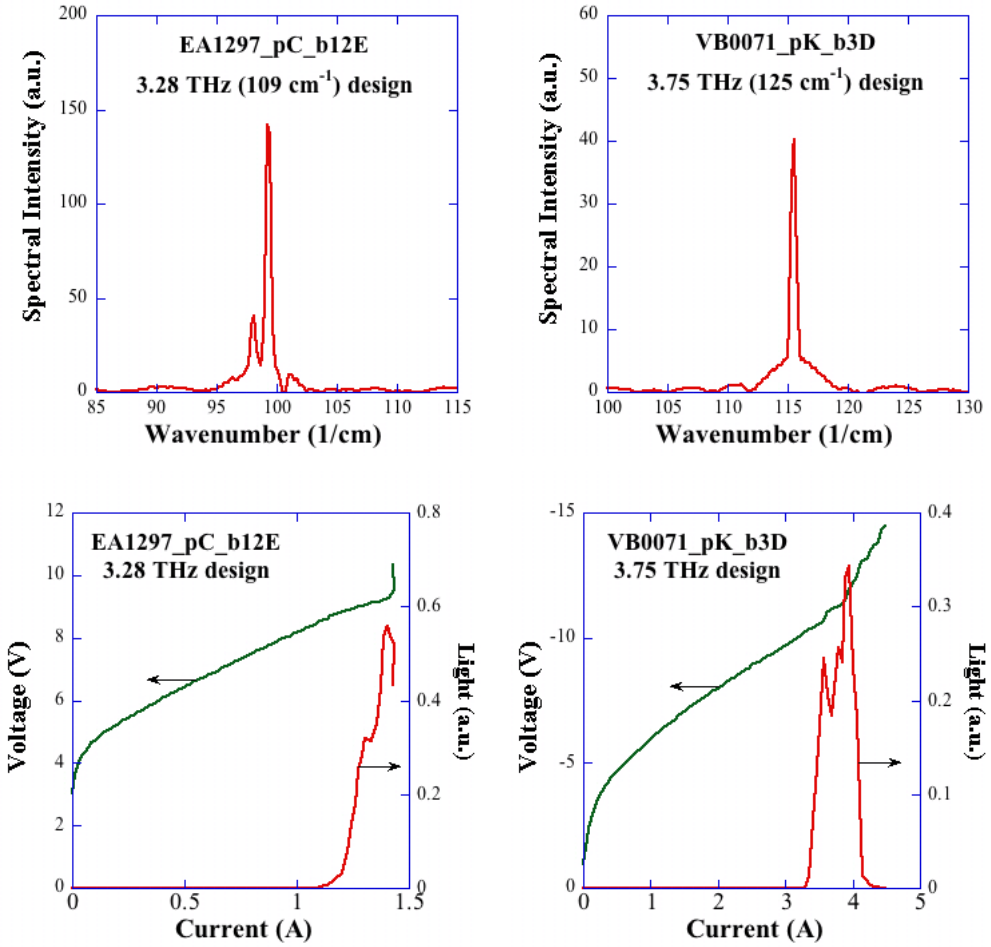

Figure 5.3. Spectra for the (a) original 3.28 THz and the (b) frequency shifted 3.75 THz designs. The voltage-light versus current relations for the (c) 3.28 THz and the (d) 3.75 THz designs.

References

[1] R. Köhler, A. Tredicucci, F. Beltram, H. E. Beere, E. H. Linfield, A. G. Davies, D. A. Ritchie, R. C. Iotti, and F. Rossi, "Terahertz semiconductor-heterostructure laser", *Nature*, vol. 417, pp.156-159, 2002.

[2] M. Rochat, L. Ajili, H. Willenberg, J. Faist, H. Beere, , G. Davies, E. Linfield, and D. Ritchie, "Low-threshold terahertz quantum-cascade lasers" , *Appl. Phys. Lett.*, vol. 81, pp. 1381-1383, 2002.

[3] B. S. Williams, H. Callebaut, S. Kumar, Q. Hu, and J. L. Reno, "3.4-THz quantum cascade laser based on longitudinal-optical-phonon scattering for depopulation," *Appl. Phys. Lett.*, vol. 82, pp. 1015-1017, Feb. 2003.

[4] R. Köhler, A. Tredicucci, C. Mauro, F. Beltram, H. E. Beere, E. H. Linfield, A. G. Davies, and D. A. Ritchie, "Terahertz quantum-cascade lasers based on an interlaced photon-phonon cascade," *Appl. Phys. Lett*, vol. 84, pp. 1266-1268, Feb. 2004.

[5] R. C. Iotti and F. Rossi, "Nature of Charge Transport in Quantum-Cascade Lasers," *Phys. Rev. Lett.*, vol. 87, pp. 1466031-466034, Oct. 2001.

[6] S. C. Lee and A. Wacker, "Nonequilibrium Greens function theory for transport and gain properties of quantum cascade structures", *Phys. Rev. B*, vol. 66, p. 245414 (2002).

[7] L. Ajili, G. Scalari, J. Faist, H. E. Beere, E. H. Linfield, A. Ritchie, and A. G. Davies, "High power quantum cascade lasers operating at lambda≈=87 and 130 μm," *Appl. Phys. Lett.*, vol. 85, pp. 3986-3988, Nov. 2004.

[8] B. S. Williams, S. Kumar, Q. Qin, and Q. Hu, "Terahertz quantum cascade lasers with double-resonant-phonon depopulation," *Appl. Phys. Lett.*, vol. 88, pp. 2611011-2611013, Jun. 2006.

[9] M. S. Vitiello, G. Scamarcio, V. Spagnolo, B. S. Williams, S. Kumar, Q. Hu, and J. L. Reno, " Measurement of subband electronic temperatures and population inversion in THz quantum-cascade lasers," *Appl. Phys. Lett*, vol. 86, pp. 1111151-1111154, Mar. 2005.

[10] S. Kumar, B. S. Williams, S. Kohen, Q. Hu, and J. L. Reno, "Continuous-wave operation of terahertz quantum-cascade lasers above liquid-nitrogen temperature," *Appl. Phys. Lett*, vol. 84, pp. 2494-2496, Apr. 2004.

[11] R. C. Iotti and F. Rossi, "Microscopic theory of hot-carrier relaxation in semiconductor-based quantum-cascade lasers," *Appl. Phys. Lett.*, vol. 76, pp. 2265-2267, Apr. 2000.

[12] A. Wacker, "Gain in quantum cascade lasers and superlattices: A quantum transport theory," *Phys. Rev. B*, vol. 66, pp.0853261-0853267, Aug. 2002.

[13] P. Harrison, D. Indjin, and R. W. Kelsall, "Electron temperature and mechanisms of hot carrier generation in quantum cascade laser," *J. Appl. Phys.*, vol. 92, pp. 6921-6923, Dec. 2002.

[14] D. Indjin, P. Harrison, R. W. Kelsall, and Z. Ikonić, "Influence of leakage current on temperature performance of GaAs/AlGaAs quantum cascade lasers," *Appl. Phys. Lett.*, vol. 81, pp. 400-402, Jul. 2002.

[15] D. Indjin, P. Harrison, R. W. Kelsall, and Z. Ikonić,"Self-consistent scattering theory of transport and output characteristics of quantum cascade lasers," *J. Appl. Phys. Lett.*, vol. 91, pp. 9019-9026, Jun. 2002.

[16] R. C. Iotti and F. Rossi, "Hot-carrier relaxation and thermalization in quantum-cascade lasers: phase coherence versus energy relaxation," *Physica B*, vol. 314, pp. 323-326, 2002.

[17] S. C. Lee and A. Wacker, "Nonequilibrium Green's function theory for transport and gain properties of quantum cascade structures," *Phys. Rev. B*, vol. 66, pp. 2453141-24531418, Dec. 2002. 6

[18] D. Indjin, P. Harrison, R. W. Kelsall, and Z. Ikonić, "Self-consistent scattering model of carrier dynamics in GaAs-AlGaAs terahertz quantum-cascade lasers," *IEEE Phot. Tech. Lett.*, vol. 15, pp. 15-17, Jan. 2003.

[19] H. Callebaut, S. Kumar, B. S. Williams, Q. Hu , and J. L Reno, "Analysis of transport properties of terahertz quantum cascade lasers," *Appl. Phys. Lett.*, vol. 83, pp. 207-209, Jul. 2003.

[20] S. C. Lee and A. Wacker, "Theoretical analysis of spectral gain in a terahertz quantum-cascade laser: Prospects for gain at 1 THz," *Appl. Phys. Lett.* vol. 83, pp. 2506-2508 ,Sept. 2003.

[21] H. Callebaut, S. Kumar, B. S. Williams, Q. Hu,and J. L Reno, "Importance of electron-impurity scattering for electron transport in terahertz quantum-cascade lasers," *Appl. Phys. Lett.*, vol. 84, pp. 645-647, Feb. 2004.

[22] Z. Ikonic, R. W. Kelsall, and P. Harrison, " Monte Carlo Simulations of Hole Dynamics in Si/SiGe Quantum Cascade Structures," *J. Computational Electronics*, vol. 1, pp. 191-194, 2002.

[23] R. C. Iotti and F. Rossi, "Microscopic theory of quantum-cascade lasers," *Semicond. Sci. Technol.*, vol. 19, pp. S323-S326, Mar. 2004.

[24] Z. Ikonic, R. W. Kelsall, and P. Harrison, "Monte Carlo simulations of hole dynamics in SiGe/Si terahertz quantum-cascade structures," *Phys. Rev. B*, vol. 69, pp. 2353081-2353089, Jun. 2004.

[25] S. C. Lee, M. Giehler, R. Hey, T. Ohtsuka, A. Wacker,and H. T. Grahn, "Dependence of lasing properties of GaAs/$Al_xGa_{1-x}As$ quantum cascade lasers on injector doping density: theory and experiment," *Semicond. Sci. Technol.*, vol. 19, pp. S45-S47 , Feb. 2004.

[26] M. F. Pereira, S. C. Lee, and A. Wacker, "Controlling many-body effects in the midinfrared gain and terahertz absorption of quantum cascade laser structures," *Phys. Rev. B*, vol. 69, pp. 2053101-2053107, May 2004.

[27] F. Banit, S. C. Lee, A. Knorr, and A. Wacker, "Self-consistent theory of the gain linewidth for quantum-cascade lasers," *Appl. Phys. Lett.*, vol. 86, pp. 0411081-0411083, Jan. 2005.

[28] O. Bonno , J. L Thobel, and F. Dessenne, "Modeling of electron-electron scattering in Monte Carlo simulation of quantum cascade lasers," *J. Appl. Phys.*, vol. 97, pp. 0437021-0437027, Jan. 2005.

[29] R. Winkler and U. Rössler, "General approach for the envelope-function approximation based on a quadrature method," *Phys. Rev. B*, vol. 48, pp. 8918-8927, Sept. 1993.

[30] R. Winkler and U. Rössler, "Multicomponent envelope function problems: the ultimate concept," *Surf. Sci.*, vol. 305, pp. 295-300 (1994).

[31] B. Robertson, "Equations of Motion in Nonequilibrium Statistical Mechanics," *Phys. Rev.*, vol. 144, pp. 151-161, Apr. 1966.

[32] I. Waldmuller, J. Forstner, S. C. Lee, A. Knorr, M. Woerner, K. Reimann, R. A Kaindl, T. Elsaesser, R. Hey, and K. H. Ploog, "Optical dephasing of coherent intersubband transitions in a quasi-two-dimensional electron gas," *Phys. Rev. B*, vol. 69, pp. 2053071-2053079, May 2004.

[33] I. Waldmueller, J. Förstner, and A. Knorr, "Self-consistent Projection Operator Theory of Intersubband Absorbance in Semiconductor Quantum Wells," in *Nonequilibrium Physics at Short Time Scales*, K. Morawetz, Ed., Berlin: Springer Verlag, 2004, pp.251-271.

[34] W. W. Chow, H. C. Schneider, S. W. Koch, C.-H. Chang, L. Chrostowski, and C. J. Chang-Hasnain, "Nonequilibrium Model for Semiconductor Laser Modulation Response," *IEEE Jour. of Quant. Elect.*, vol. 38, pp. 402-409, Apr. 2002.

[35] P. Harrison, "The nature of electron distribution functions in quantum cascade lasers," *Appl. Phys. Lett*, vol. 75, pp. 2800-2802, Nov. 1999.

[36] U. Ekenberg, "Nonparabolicity effects in a quantum well: Sublevel shift, parallel mass, and Landau levels," *Phys. Rev. B*, vol. 40, pp. 7714-7726, Oct. 1989.

[37] J. Li and C. Z. Ning, "Effects of electron-electron and electron-phonon scatterings on the linewidths of intersubband transitions in a quantum well," *Phys. Rev. B.*, vol. 70, pp. 1253091-1253098, Sept. 2004.

[38] C. Gmachl, F. Capasso, A. Tredicucci, D. L. Sivco, R. Khler, A. L. Hutchinson, and A. Y. Cho," Dependence of the device performance on the number of stages in quantum-cascade lasers," *IEEE JSTQE*, vol. 5, pp. 808-816, May/Jun 1999.

[39] D. Nikonov, A. Imamoglu, L. V. Butov, and H. Schmidt, "Collective Intersubband Excitations in Quantum Wells: Coulomb Interaction versus Subband Dispersion," *Phys. Rev. Lett.*, vol. 79, pp. 4633-4636, Dec. 1997.

[40] I. Waldmuller, M. Woerner, J. Forstner, and A. Knorr, " Theory of the lineshape of quantum well intersubband transitions: optical dephasing and light propagation effects," *Phys. Status Solidi B*, vol. 238, pp. 474-477, Jul. 2003.

[41] J. Li and C. Z. Ning, "Interplay of Collective Excitations in Quantum-Well Intersubband Resonances," *Phys. Rev. Lett.*, vol. 91, pp. 0974011-0974014, Aug. 2003.

[42] V. D. Jovanovic, D. Indjin, N. Vukmirovic, Z. Ikonic, P. Harrison, E. H. Linfield, H. Page, X. Marcadet, C. Sirtori, C. Worrall, H. E. Beere, and D. A. Ritchie, "Mechanisms of dynamic range limitations in GaAs/AlGaAs quantum-cascade lasers: Influence of injector doping," *Appl. Phys. Lett.*, vol. 86, pp. 2111171-2111173, May 2005.

[43] O. Gauthier-Lafaye, et al., Appl. Phys. Lett., **74**, 1537 (1999)

[44] H.C. Liu, et al., Phys. Rev. Lett., **90**, 077402 (2003)

[45] M. Troccoli, et al., Nature, **433**, 845 (2005)

[46] Owschimikow, et al., Phys. Rev. Lett., **90**, 043902 (2003)

[47] C. Gmachl, et al., IEEE J. Quant. Electron., **39**, 1345 (2003)

[48] S.S. Dhillon, et al., Appl. Phys. Lett., **87**, 071101 (2005)

[49] Y. Shimada, et al., Phys. Rev. Lett., **90**, 046806 (2003)

[50] A. Zhang, et el., Appl. Phys. Lett., **86**, 171110 (2005)

[51] I. Waldmueller, et al., IEEE JQE, **42**, 292 (2006)

[52] M. O. Scully and M. S. Zubairy, *Quantum Optics* (University Press, Cambridge, 1997)

[53] R. Ascazubi, et al., Appl. Phys. Lett., **81**, 4344 (2002)

[54] A. Liu and C.Z. Ning, Appl. Phys. Lett., **75** 1207 (1999)

[55] J.M. Hensley et. al., *Optical Terahertz Science and Technology Topical Meeting and Exhibition* (2007)

[56] L. Ajili et al., *Electron. Lett.*, **38**, 1675 (2002)

[57] A. Barkan et al., *Opt. lett.*, **29**, 575 (2004)

[58] L. Mahler et al., *Appl. Phys. Lett.*, **84**, 5446 (2004)

[59] S. Golka et al., *Appl. Phys. Lett.*, **86**, 111103 (2005)

[60] A.W.M. Lee et al., *Appl. Phys. Lett.*, **89**, 141125 (2006)

[61] H.E. Beere et al., *J. Crystal Growth*, **301**, 935 (2007)

[62] J. Freeman et al., *ITQW07* (2007)

[63] S. Kumar et al., *ITQW07* (2007)

[64] B.S. Williams et al., *Electron. Lett.*, **42**, 89 (2006)

Appendix A

Frequency shifting Algorithm

The following is the algorithm for automatic frequency-shifting QCL design program. The analyze structure subroutine first analyzes a QCL structure of interest and generates a set of anticrossing and coupling splitting energies of two neighboring quantum wells throughout the whole structure. The reverse engineer subroutine then determines the new applied electric field, and generates a structure with the same values of anticrossing and coupling splitting energies except the pair which determine the optical transition energy.

1. Enter a known structure (Fig. A.1)
2. Compute the anticrossing and coupling splitting energies for each pair of neighboring wells
3. Adjust some of the anticrossing and coupling splitting energy values to modify the optical transition energy
4. Use the electric field and the first well width of the original structure as the starting point and set $w_{1old} = w_1$
5. With the most recent well width (w_n) determine the widths of the barrier (b_{n+1}) and the next neighboring well (w_{n+1}), which will result in desirable anticrossing and coupling splitting energies ($asgoal_n$ and $csgoal_n$) via the Newton's method (Fig. A.2)
6. Repeat step 5 until the last and the first well widths (w_{last}, w_{1new}) are found
7. If $|w_{1new} - w_{1old}| <$ tolerant (0.0001 eV), the program is terminated, else adjust the electric field, set $w_{1old} = w_1$, and repeat step 5 - step 7

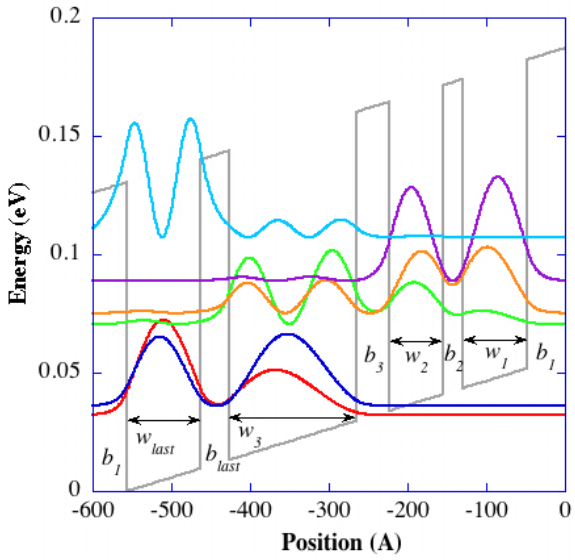

Figure A.1. An example of a QCL structure of interest: coupled quantum-wells design. First, The anticrossing and coupling splitting energies from all the neighboring well ((w_1, w_2), (w_2, w_3), (w_3, w_4), and (w_4, w_1)) are determined via the analyze structure subroutine. Later, the anticrossing and coupling splitting energies between w_1 and w_2 are modified to adjust the optical transition energy.

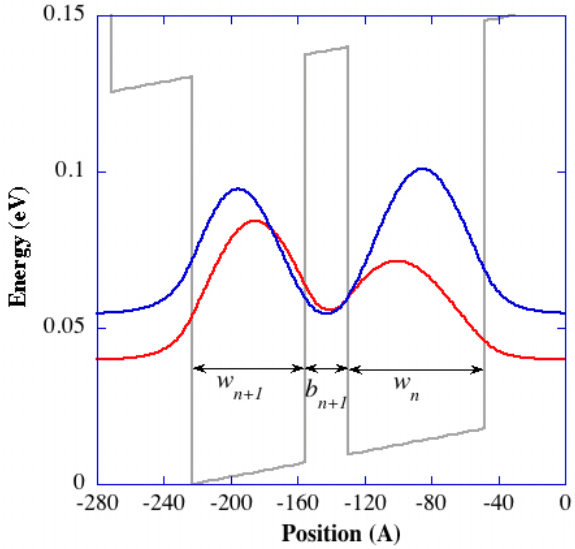

Figure A.2. For a given well width (w_n) and a pair of anticrossing and coupling splitting energies constrains, the reverse engineering program generates the neighboring barrier (b_{n+1}) and quantum well (w_{n+1}), which satisfy the constraints.

DISTRIBUTION:

1	MS 0406	Toby Townsend, 5713
1	MS 1071	Andy Boye, 1720
1	MS 1082	Jim Hudgens, 1725
2	MS 1082	Mike Wanke, 1725
1	MS 1082	Maytee Lerttamrab, 1725
1	MS 1086	Ines Waldmueller, 1123
1	MS 1086	Weng Chow, 1123
1	MS 0899	Technical Library, 9536 (electronic copy)
1	MS 0123	D.L. Chavez, LDRD Office, 1011